Multi-decadal Dutch coastal dynamic mapping with multi-source remote sensing imagery

Zhang, Bin; Chang, Ling; Wang, Zhengbing; Wang, Li; Ye, Qinghua; Stein, Alfred

DOI
10.1016/j.jag.2025.104452

Publication date
2025

Document Version
Final published version

Published in
International Journal of Applied Earth Observation and Geoinformation

International Journal of Applied Earth Observation and Geoinformation 138 (2025) 104452

Contents lists available at ScienceDirect

International Journal of Applied Earth Observation and Geoinformation

journal homepage: www.elsevier.com/locate/jag

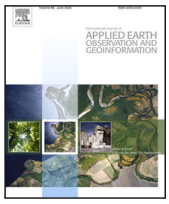

Multi-decadal Dutch coastal dynamic mapping with multi-source remote sensing imagery

Bin Zhang [a,b,*], Ling Chang [a], Zhengbing Wang [c,d], Li Wang [e], Qinghua Ye [c,d], Alfred Stein [a]

[a] Faculty of Geo-Information Science and Earth Observation (ITC), University of Twente, Enschede, The Netherlands
[b] College of Geological and Surveying Engineering, Taiyuan University of Technology, Taiyuan, China
[c] Faculty of Civil Engineering and Geosciences, Delft University of Technology, Delft, The Netherlands
[d] Deltares, Delft, The Netherlands
[e] International Marine and Dredging Consultants, Antwerp, Belgium

ARTICLE INFO

Keywords:
SAR and optical imagery
Polarization
Object-Based Image Segmentation
Tidal flat DEM
Dutch Wadden Sea

ABSTRACT

Tidal flats and their associated sandbanks are dynamic environments crucial for ecological balance and biodiversity. Monitoring their evolutionary history and topographic changes is important to better understand their dynamic mechanisms and predict their future status. Accurately mapping their evolution, however, remains challenging due to highly dynamic currents, suspended sediment variability, and unclear boundaries between land, tidal flats, and water. Traditional waterline methods struggle under these conditions. In this study, we propose an Object-Based Image Segmentation (OBIS) method, specifically designed for SAR images, to extract waterlines and distinguish tidal flats and shorelines from water bodies. This method integrates SAR polarimetric feature analysis to select high-quality images and employs partition processing to preserve local feature statistics. Using 199 Sentinel-1 GRD, 132 Radarsat-2 SLC, and 157 Landsat images, we analyzed coastal dynamics in the Dutch Wadden Sea from 1986 to 2020. Our DEMs, validated against LiDAR data (2016–2019) and 58 ground anchor measuring stations (2011–2020), achieved an accuracy of 10–30 cm. Results show that coastal tidal flats and sandbanks expanded at rates of 0.107–0.324 $km^2\ yr^{-1}$ and 0.010–0.073 $km^2\ yr^{-1}$, respectively, with a net intertidal volume increase of approximately $8.6\times10^7\ m^3$. The generated DEMs provide valuable insights for sediment budget evaluation and hydrodynamic modeling, supporting scientific research and coastal management. The proposed OBIS-based framework demonstrates its effectiveness for mapping national-scale tidal flats and sandbanks dynamics.

1. Introduction

Tidal flats are parts of the sea that are partly inundated at high tides and are exposed to air during low tides. Such a dynamic environment creates complex landforms and provides habitats for a high diversity of aquatic and terrestrial species (Kabat et al., 2012). A tidal flat has a unique ecosystem, while it also serves as an essential base for aquaculture and the development of agricultural production (Reise et al., 2010). Various factors, however, result in an ongoing decline in these ecosystems worldwide, e.g., coastal development, reduced sediment delivery from major rivers, sinking of riverine deltas, increased coastal erosion, pollution, and sea-level rise. The total area of tidal flats in East Asia, the Middle East and North America has thus decreased by 16% from 1984 to 2016 (Murray et al., 2019) and the global wetlands declined by 4000 km^2 between 1999 and 2019 (Murray et al., 2022). Apart from tidal flats, sandbanks play a crucial role in coastal sedimentary systems, influencing sediment transport, hydrodynamics, and ecosystem stability. They influence tidal currents and sediment deposition, shaping the intertidal zone over time. Continuously obtaining and monitoring their topography is important to understand their evolutionary history, forecast their development, and inform a wide range of potential management actions to maintain these areas.

To address this need, several geodetic-based topographic mapping techniques have been proposed. Traditional ground and ship-based surveys, such as GPS and leveling, provide measures with high accuracy (1–5 cm for vertical and positional measurements) (Gorman et al., 1998) and repeatability, but they are labor-intensive, costly, and offer limited spatial coverage. Airborne LiDAR enables rapid, dense-grid elevation mapping with centimeter-level vertical and decimeter-level horizontal precision; however, it is expensive and heavily dependent

* Corresponding author at: Faculty of Geo-Information Science and Earth Observation (ITC), University of Twente, Enschede, The Netherlands.
E-mail addresses: binzhang@tyut.edu.cn (B. Zhang), ling.chang@utwente.nl (L. Chang), z.b.wang@tudelft.nl (Z. Wang), li.wang@imdc.be (L. Wang), qinghua.ye@deltares.nl (Q. Ye), a.stein@utwente.nl (A. Stein).

https://doi.org/10.1016/j.jag.2025.104452
Received 10 December 2024; Received in revised form 4 February 2025; Accepted 26 February 2025
Available online 13 March 2025

on favorable weather conditions, and it faces challenges in achieving large-area coverage (Chust et al., 2008; Yang et al., 2023). Radar altimetry, though effective for surface height measurements, is constrained by low spatial resolution (e.g., 5 km for ERS-1 and 250 m for CryoSat) (Da Silva et al., 2010; Foresta et al., 2018), rendering it unsuitable for small-scale studies. Interferometric Synthetic Aperture Radar (InSAR), utilizing phase information, is effective for generating tidal flat digital elevation models (DEMs) (Lee and Ryu, 2017; Choi and Kim, 2018), but traditional multi-pass interferometry is hampered by phase decorrelation (Zhang et al., 2021a, 2022a), and data from bistatic-mode SAR systems like TanDEM-X are not typically freely accessible. UAVs, while capable of producing centimeter-level DEMs and improving waterline extraction accuracy by 51% (Kalacska et al., 2017; Chen et al., 2023a), have limitations in endurance and wind resistance, restricting their ability to cover extensive tidal flat areas.

The emergence of the waterline method provided an economical, efficient, and relatively accurate way to create a DEM of intertidal zones (Mason et al., 1995). The waterline method uses remote sensing images, including optical or Synthetic Aperture Radar (SAR) images, to extract the waterline, defined as the ever-shifting boundary between tidal flats and adjacent water areas. The position of the boundary is considered a topographical quasi-contour line but is not an actual contour line because the water level of the tidal wave varies horizontally (Kang et al., 2017). Using the water level as the altimeter, its value is assigned to every waterline. These waterlines with water level heights are assembled and interpolated to produce a DEM. The waterline method has been successfully used for several studies, for instance, over the Humber/Wash area (Mason et al., 1995), the German Wadden Sea (Niedermeier et al., 2005; Heygster et al., 2009; Li et al., 2014), the northern coast of Vietnam (Tong et al., 2020), and the Beibu Gulf (Gao et al., 2024).

As one of the primary data sources, SAR images offer several advantages over optical images, such as all-weather capability and a high revisit frequency, making them particularly suitable for the waterline method. Due to its extensive area coverage, however, SAR images are easily influenced by ocean waves and suspended sediment (Collard et al., 2005; Shao et al., 2021). It leads to a weak contrast in the backscatter coefficient, making distinguishing water and tidal flats difficult. Also the dielectric constant and soil moisture influence the backscatter coefficient values of tidal flats (Kim et al., 2013). So far it has been unexplored how to mitigate these disturbing factors efficiently using SAR data with multi-polarization.

A key step of the waterline method is edge detection. Traditional edge detection methods like the wavelet-based algorithm (Heygster et al., 2009), the region-based and edge-based active contour models (Liu et al., 2017), the thresholding method (Wang et al., 2020) and *k*-means clustering (Soares et al., 2012) suffer from the edge pixels produced by edge detectors and hence show discontinuities and rarely characterize a waterline completely (Zhang et al., 2022b). The Otsu algorithm is a popular method, automatically selecting the optimal threshold by maximizing inter-class variance. However, it may struggle with complex or noisy images (Chen et al., 2024). Also, speckle noise in SAR images influences the edge detection accuracy for pixel-based methods (Niedermeier et al., 2005). New methods for waterline extraction based upon machine learning methods include a holistically nested edge detection network (HED) (Baumhoer et al., 2019), U-Net (Heidler et al., 2021) and WENet (Zhang et al., 2022b). Such methods, however, require intensive label data preparation and are less suited when data are only available to a limited degree. Object-based analysis methods have their advantages in delineating object boundaries and reducing "salt and pepper" effects (Jung et al., 2015; Mao et al., 2020). These have not yet been explored for waterline extraction in tidal flats.

Compared to the waterline method, the emerging water frequency method leverages full-time series remote sensing imagery for more comprehensive tidal sampling and mitigates the uncertainties associated with waterline extraction, making it increasingly attractive to researchers (Jia et al., 2021; Chen et al., 2023b; Wu et al., 2024). A key prerequisite for successfully applying this method is the availability of sufficient remote sensing imagery. This, however, is challenging to achieve in most cases. Therefore, until remote sensing data become sufficiently abundant on a global scale, the waterline method will remain the most effective and widely used method.

This research proposes a generic scheme to extract tidal flats and create the corresponding DEM in a highly dynamic sea environment. We focus on the Dutch Wadden Sea that is bounded by a coastline of 170 km as the southern edge of the five islands, 135 km as the northern part of the mainland and a dynamic coastline extent along uninhabited sandbanks and islands. Three ideas support the scheme: (1) object-based segmentation to distinguish the morphological pattern of tidal flats; (2) using SAR polarimetric features to distinguish and remove the corresponding land areas, resulting in reducing multi-mode images to bi-mode images before using object-based segmentation; (3) separating the research area into multiple patches based upon their spatial discontinuity by partition processing to mitigate the heterogeneity of an image, thereby improving object-based segmentation accuracy. This scheme is used to create the DEM of the intertidal zone in the Dutch Wadden Sea. Besides, we implemented a test to compare the performance of two water level simulation models: Delft3D Flexible Mesh and TPXO. This research aims to enhance our understanding of Dutch tidal flat dynamics, contribute to its sustainable management, and provide valuable insights for informed decision-making in coastal conservation and development planning.

2. Study area and data sources

2.1. Study area

The Wadden Sea is the most extensive tidal flat in the world (Fig. 1(a)). It spans 500 km along the coasts of Denmark, Germany, and the Netherlands (Wang et al., 2018a). Due to storms and changes in sea level, the geomorphology of the Wadden Sea is very dynamic. Its sediments are mainly supplied from the adjacent sea with only minor river influences locally (Reise et al., 2010). The complex and dynamic Wadden Sea habitats accommodate a high diversity of aquatic and terrestrial species. e.g., more than 10,000 species of flora and fauna are found in this area (CWSS, 2020).

Our study area is located in the Dutch part of the Wadden Sea marked with the green square in Fig. 1(a). It is located between the Marsdiep off Den Helder and the Dollard in Groningen. It is surrounded by five islands (i.e., Texel, Vlieland, Terschelling, Ameland and Schiermonnikoog) and four small sandbanks (i.e., Noorderhaaks, Rottumerplaat, Rottumeroog and Zuiderduintjes) (see Fig. 1(d)). The area is divided into ten tidal inlet systems marked with white lines in Fig. 1(a). Every inlet system consists of relatively sizeable ebb-tidal delta shoals, narrow and deep inlet channels, and tidal flats (Van Prooijen et al., 2020; FitzGerald, 1996). The length of the Dutch Wadden Sea in the West-East direction is approximately 180 km, and the distance from land to the five islands ranges from approximately 6 km to 30 km.

The tidal flats in the Dutch Wadden Sea consist of sand (~90%, grain size 0.1–0.2 mm) and fine-grained muddy sediments (~10%) with decreasing grain sizes away from the inlet, while ebb-tidal deltas primarily consist of sand (0.1–0.4 mm), which is finer on the shoals and coarser in the channels (Lodder et al., 2019; Alonso et al., 2021).

2.2. Data sources

This study combines radar and optical remote sensing images, and the results are validated with ground anchor measuring and LiDAR data.

(1) Remote sensing imagery

Two types of SAR images, i.e., Ground Range Detected (GRD) for Sentinel-1A/B with VV/VH polarization modes and Single-Look Complex (SLC) for Radarsat −2 with HH/HV polarization modes, one type

Table 1
Basic parameters of SAR and optical imagery used for this study. Des indicates descending, while Asc indicates ascending. Track represents the satellite image orbit number. Nr. represents the number of available images in this study. Time is the approximate data acquisition time (UTC).

Missions	Format	Direction	Track	Date	Time	Nr.	Pixel size
Sentinel-1A	GRD	Des	415	Nov. 2016–Dec. 2020	5:50	112	10 m × 10 m
Sentinel-1B	GRD	Asc	171	Jun. 2017–Dec. 2020	17:25	87	10 m × 10 m
Radarsat-2	SLC	Des	202	Feb. 2011–Dec. 2015	5:57	70	12 m × 5 m
Radarsat-2	SLC	Des	302	Feb. 2011–Jul. 2015	5:53	62	12 m × 5 m
Landsat-8 OLI	GeoTIFF	Des	198	Mar. 2014–Sep. 2020	10:33	29	30 m × 30 m
Landsat-7 ETM+	GeoTIFF	Des	198	Jul. 1999–Apr. 2020	10:30	54	30 m × 30 m
Landsat-5 TM	GeoTIFF	Des	198	Feb. 1986–Apr. 2011	10:10	74	30 m × 30 m

of optical images with less-than-20% cloud coverage were used. Their specific information is summarized in Tables 1 and 9 in Appendix A.

(2) Validation data

Measured elevation data, w.r.t. the NAP (Normaal Amsterdams Peil, the Dutch vertical datum), of 58 ground anchor measuring stations from 2011 to 2020 were collected. The NAP is defined as approximately the mean water level for Amsterdam in the absence of water motion. Differences with respect to Mean Sea Level (MSL) are caused by meteorological and oceanographic influences. Their locations are displayed with the yellow dots in Fig. 1(d). The LiDAR data from 2016, 2017, 2018 and 2019 with a 2 m × 2 m spatial resolution were collected from Rijkswaterstaat (Arens et al., 2013) and its density is about 3-10 points m^{-2}. The horizontal and vertical accuracies of the LiDAR data were approximately 20 cm and 10 cm, respectively. The data were processed using the UTM Zone 31N coordinate system, with NAP serving as the vertical datum. Each LiDAR dataset covers approximately 25% of the study area and was collected at a relatively low tide.

3. Methods

Section 3.1 introduces the standard procedures to enhance the contrast of SAR and optical data and convert them into the same format. We then present a new method to select high-quality SAR images for tidal flats based upon polarimetric features. Section 3.2 describes the way to extract shorelines and waterlines based upon OBIS (Object-Based Image Segmentation) or natural spatial discontinuity. In Section 3.3, we use two water level simulation models to hindcast water level information. Section 3.4 shows the procedure of DEM creation. The methods used to analyze the evolution features and validate the results are discussed in Section 3.5 and Section 3.6. The overall procedures are displayed in Fig. 2.

3.1. Data pre-processing

All satellite data are inevitably affected by the noise and some did not capture the exposed tidal flats. Besides, they were recorded in distinct reference coordinates and have different pixel spacings. Therefore, standard image pre-processing needs to be implemented before using all remote sensing images for waterline and shoreline extraction. Section 3.1.1 describes the steps to produce the backscatter coefficient images from GRD and SLC data and Normalized Difference Water Index (NDWI) images from optical data. These steps aim to enhance the contrast of tidal flats, land and water, which serves to detect the edges of the tidal flats in Section 3.2. Section 3.1.2 shows a proposed method to further identify high-quality SAR images using the SAR polarimetric features.

3.1.1. Image enhancement

Pre-processing for Sentinel-1A/B SAR GRD images (see Fig. 2) includes seven steps: (1) Orbit correction: the precise positioning data is used to improve orbit accuracy. It is beneficial for improving geolocation accuracy. (2) Reduction of thermal noise: thermal noise produced by SAR satellite devices (transmitters, power amplifiers and receivers) influences radar backscatter signal accuracy and is reduced by the operational ESA Instrument Processing Facility (IPF). (3) Radiometric calibration: Sentinel-1 Level 1 images are generally not radiometrically corrected and have significant radiometric bias. The radar backscatter coefficient value needs to be re-calibrated for each pixel based upon an external DEM. (4) Multi-looking: to suppress speckle noise, we used three range/azimuth looks to keep the same pixel spacing with optical images (e.g., 30 m). (5) Speckle-filtering: we used a Refined Lee filtering method with a 3 × 3 kernel to remove speckle. (6) Orthorectification: SAR is a side-view imaging. The fluctuation of the terrain causes geometric distortion to the SAR image that we corrected using the range-Doppler terrain correction method with a DEM (e.g., SRTM 3arc-second). (7) Logarithmic conversion: $\sigma^0(\mathrm{dB}) = 10\log_{10}(\sigma^0)$ as the range of the logarithmic radar backscatter coefficient is better approximated by the Gaussian distribution, the number of data storage bits is reduced because double-precision data can be stored as floats and logarithmically converted coefficients provide more convenient visualization.

For Radarsat −2 SAR SLC images, the pre-processing (see Fig. 2) includes five steps: (1) Intensity computation: the complex value per pixel in SLC is converted into intensity value by $A^2 = (\mathrm{Re}\{Z\})^2 + (\mathrm{Im}\{Z\})^2$ where Z is a complex phasor per pixel ($Z = A\exp(j\psi)$, ψ being the received radar signal phase, j the imaginary unit, A the amplitude, and Re{.} and Im{.} represent the real and imaginary part of the phasor, respectively) (Hanssen, 2001). (2) Resampling: the intensity images are resampled to the same pixel spacing as optical images (e.g., 30 m) using a bilinear interpolation method. (3) Speckle-filtering, (4) Orthorectification and (5) Logarithmic conversion are three same steps as steps (5)–(7) for the Sentinel-1 GRD images.

For the optical images, the performance of the Landsat cloud mask product is unsatisfactory. Therefore, we manually discarded the images with clouds covering the research area by visual interpretation (see Fig. 2). Because of the failure of the Scan Line Corrector of Landsat −7 on 31 May 2003, its images have gaps. The localized linear histogram matching method developed by USGS/NASA was used to fill the gaps (Asare et al., 2020). The Normalized Difference Water Index (NDWI) (McFeeters, 1996; Salameh et al., 2020) was applied to discern between water and nonwater, and water and tidal flats, defined as:

$$\mathrm{NDWI} = \frac{B_{green} - B_{NIR}}{B_{green} + B_{NIR}}, \quad (1)$$

where B_{green} and B_{NIR} means the reflectances of the green and the Near Infra-Red (NIR) bands. B_{green} and B_{NIR} for Landsat −8 are spectral bands 3 and 5, while for Landsat −5 and −7 these are the spectral bands 2 and 4. After this step, we reprojected the pixels into the WGS84 coordinate reference system.

After this pre-processing, the images have a uniform pixel spacing equal to 30 m and are in a common coordinate system (i.e., WGS_1984_UTM_Zone_31N), and the differences between land, tidal flats, and water are enhanced.

3.1.2. Exclusion of noisy and invalid images

Two tidal cycles take place every 24 hrs 50 mins in the Dutch Wadden Sea. The extra 50 mins with respect to 24 h per solar day, leads to the cycle slip of the tide pattern day by day (Chang and Stein, 2021). Consequently, SAR and optical images capture different phases of tides, even though the revisit time of SAR and optical images in any area is

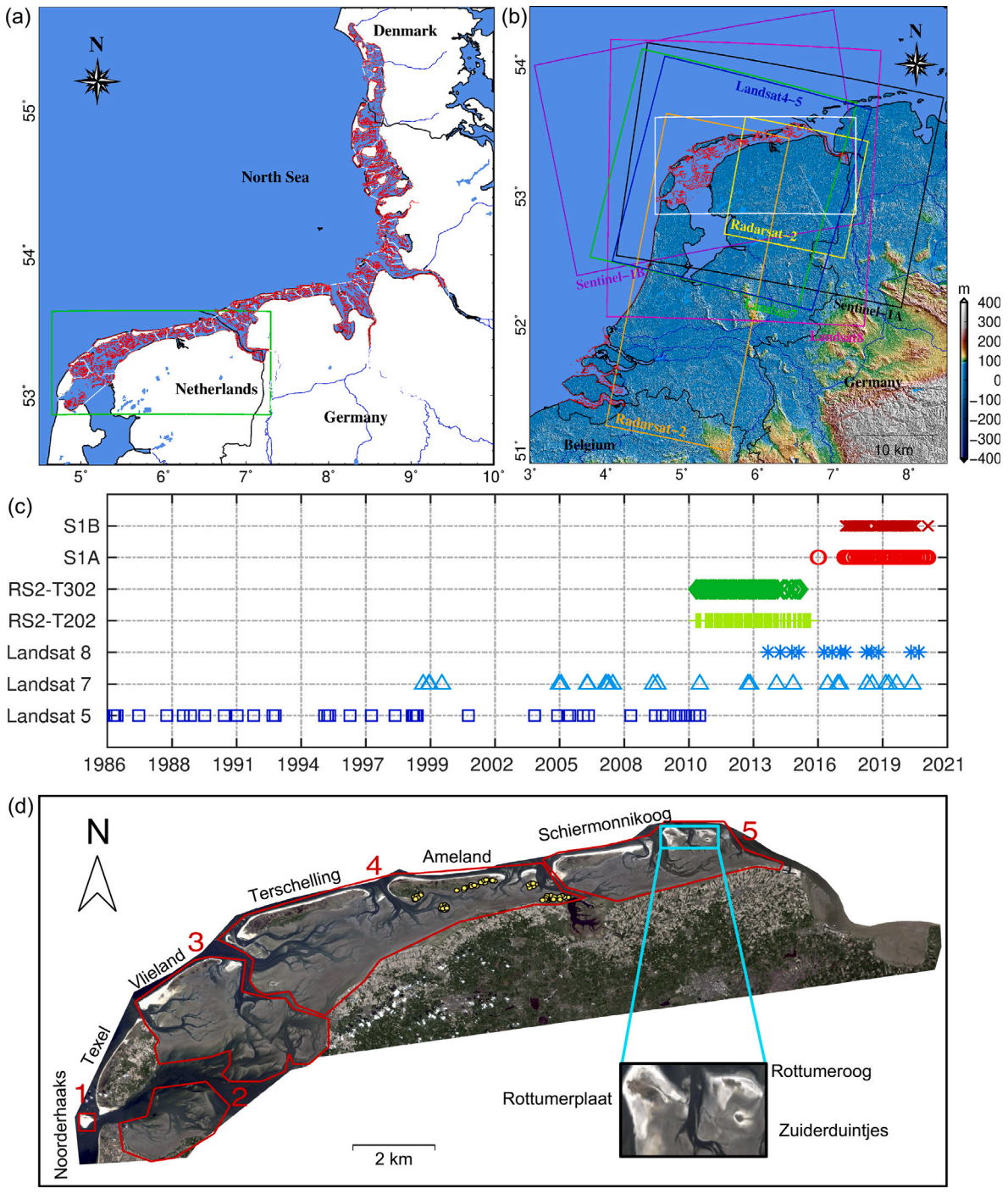

Fig. 1. (a) The map of the entire Wadden Sea and the Dutch Wadden Sea as the study area marked with a green square. Red lines indicate the location of tidal flats in the Wadden Sea. (b) Spatial coverage and (c) time distribution of Sentinel-1A/B (S1A/S1B), Radarsat −2 (RS2), Landsat −8, Landsat −7 and Landsat −5 data. (d) Research area superimposed on a Landsat −7 image captured on 20 April 2009. The white square in subfigure(b) indicates the study area. The red lines represent the boundaries of five patches based upon natural spatial discontinuity in subfigure(d). The yellow dots indicate the locations of 58 ground anchor measuring stations. Five islands (Texel, Vlieland, Terschelling, Ameland and Schiermonnikoog) and four sandbanks (Noorderhaaks, Rottumerplaat, Rottumeroog and Zuiderduintjes) are discussed in Sections 4.2 and 4.3. (For interpretation of the references to color in this figure legend, the reader is referred to the web version of this article.)

relatively constant. Among them, part of the images do not capture the exposed tidal flats, which are considered as invalid images and are excluded. Furthermore, we treat the SAR images that are heavily polluted by speckle noise as noisy images, and discard them as well.

We now present our method to exclude noisy and invalid SAR images based upon the polarimetric features (see Fig. 2). First, we exclude the noisy images. Cloudy optical images have been excluded in Section 3.1.1 and therefore we focus on the SAR images. When the histogram of a co-polarization SAR image has a single peak, this image is considered as a heavily polluted image by noise and is excluded (Salameh et al., 2020). The reason is that the harsh noise causes a low contrast between different surface types (e.g., land and water). They are considered less-noisy images when they have two peaks and would be used for further selection in the next step. Next, we remove the images with submerged tidal flats. For optical images, because of their small amount, invalid images are excluded on the basis of visual

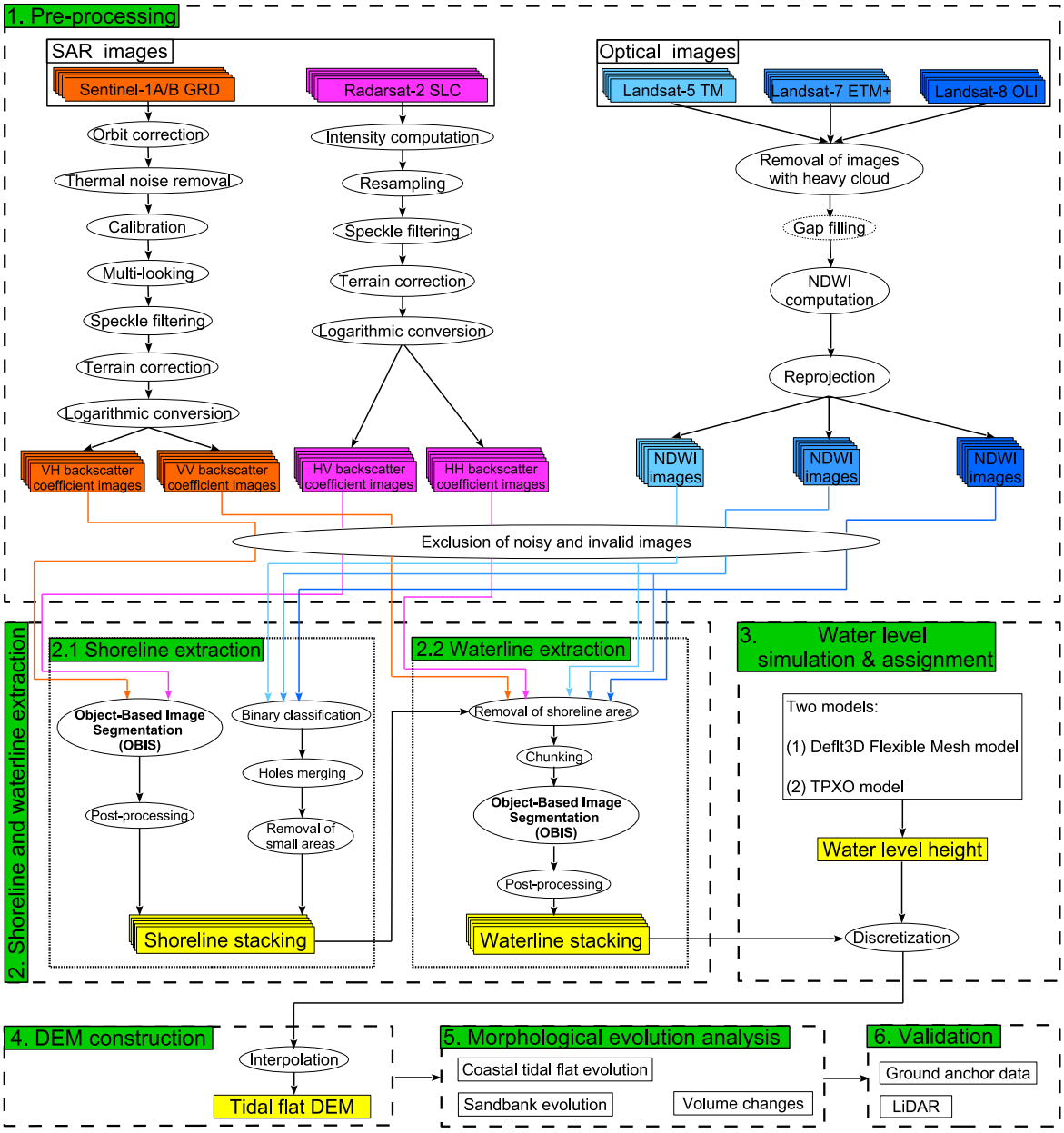

Fig. 2. The block diagram of the data processing and analysis for this study.

interpretation. For SAR images, we compare their histogram with co- and cross-polarization. When the value of the lowest point between the two peaks from the co-polarization SAR image is much larger than that from the cross-polarization SAR image (e.g., the red and pink points in Fig. 3), the tidal flats in the images are exposed, and the image is valid to be used. In contrast, when the values of the lowest point between the two peaks from co- and cross-polarization SAR images are almost the same (e.g., the blue and cyan points in Fig. 3), the tidal flats in the SAR image are submerged. The reason is that co-polarized radar signals are more sensitive to smooth, regular surfaces like water or wetlands, whereas cross-polarized signals are superior in detecting surface roughness, vegetation, or structural irregularities. After these two steps, the high-quality images are identified and can be used for waterline extraction in the next step.

3.2. Shoreline and waterline extraction

3.2.1. Object-based image segmentation method

Object-Based Image Segmentation (OBIS) is an iterative method that starts with the segmentation of images into homogeneous and contiguous image segments (also called image objects) (Blaschke, 2010; Hossain and Chen, 2019). As the most popular OBIS method (Belgiu and Csillik, 2018; Wang et al., 2018b), multi-resolution segmentation is used in this study. Multi-resolution segmentation is a region-growing algorithm that starts from the pixel level and iteratively aggregates pixels into objects until the conditions of homogeneity imposed by the user are met (Baatz, 2000). Multi-resolution segmentation relies on three parameters: scale, shape and compactness. The scale parameter dictates the size and homogeneity of the resultant objects. The larger value produces larger objects. The shape parameter determines the

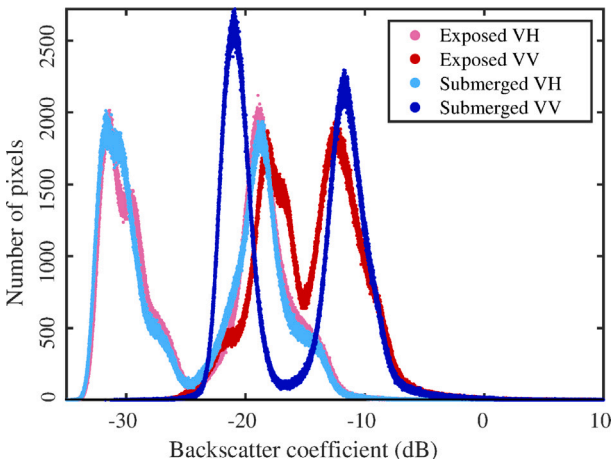

Fig. 3. Histogram of the pixel backscatter coefficient for co- and cross-polarization (VV and VH) SAR images with exposed (in red and pink) and submerged (in blue and cyan) tidal flats. The SAR images from Sentinel-1 A with exposed and submerged tidal flats were acquired on 12 April 2016 and 19 March 2016. (For interpretation of the references to color in this figure legend, the reader is referred to the web version of this article.)

degree of influence of the radiometry versus the object shape during the delineation of the image objects. The shape parameter ranges between 0 and 1: smaller values result in objects that are optimized for radiometric homogeneity, and higher values generate objects that are optimized for shape homogeneity (Esch et al., 2008). The compactness parameter also varies between 0 and 1, determining the degree of smoothing of the object's borders. A reasonable combination of parameters obtained after optimization yields sensible segmentation results.

Parameter optimization selection has been a research topic over the last decades. Some automatically optimal parameter determination procedures were proposed (Chen et al., 2018). They, however, are more suitable for cases whose features have stable shapes. Tidal flats have irregular morphological features and are constantly evolving. Determining an optimal parameter combination for all research patches is difficult. Therefore, the human-driven trial-and-error method is applied in this research. Empirical parameters are recommended, e.g., a small shape parameter of 0.1. The set of scale and compactness parameters is different with regard to different research targets, e.g., shoreline and waterline, and vary many from 10 to 500 and from 0.1 to 0.9. In our study, the OBIS method is separately applied in shoreline extraction for cross-polarization SAR images (see Section 3.2.2) and waterline extraction (see Section 3.2.3).

3.2.2. Shoreline extraction

The shoreline is a precise and dynamic line between land and water that fluctuates with immediate water levels. In contrast, the coastline serves as a broader and more stable reference, marking the landward edge of the coastal zone and typically defined at the mean high-water line (Chen et al., 2019). Shoreline area and water exhibit distinct features in a SAR image with different polarization modes, e.g., co- and cross-polarization, because of different surface roughness and dielectric constant. With VV or HH co-polarization, land area and water have strong backscattering. Nevertheless, with VH or HV cross-polarization, the land area has a stable and robust backscattering, while water has almost no reflection. This is because the land surface is rough and therefore exhibits volume scattering. The polarization effect weakens the received signal, but some echo signals will still be received, while the water surface is relatively smooth, so it exhibits specular scattering. Such a polarization effect will further weaken the already low echo signal to none. Therefore, we define a two-step procedure (see Fig. 2) to extract shorelines from SAR images.

Step 1: Use cross-polarization SAR images to distinguish water and land area and employ a multi-resolution segmentation algorithm to extract the shoreline. Because of the strong contrast between land area and water in these images, a large scale parameter (e.g., 350) and compactness parameter (e.g., 0.9) are set up.

Step 2: Carry out post-processing to remove the inaccurate segmentation. This processing step is straightforward due to the significant backscattering difference between land area and water in cross-polarization SAR images.

For optical images, we define a three-step procedure (see Fig. 2) to extract shorelines from the NDWI images produced in Section 3.1.1.

Step 1: Execute binary classification by Jenks natural breaks method (Jenks, 1967)for land and non-land areas in the NDWI images. Leveraging the unique characteristics of each image, the method minimizes intra-group variance and maximizes inter-group differences to partition the data into two categories, effectively representing its distributional properties.

Step 2: Reclassify the holes in land areas and label them as the land. These holes are caused by their pixels' NDWI values and are similar to the water NDWI value. Some of these holes can be ponds on the land area.

Step 3: Remove small areas in the non-land area that usually correspond to noisy features caused by incorrect segmentation results. Since the Zuiderduintjes sandbank (see Fig. 1(d)) is the smallest study object with a spatial extent of 0.07 km^2, we define an area below 0.07 km^2 as a small area.

3.2.3. Waterline extraction

Using the produced shorelines (Section 3.2.2), we define a four-step procedure to extract waterlines (see Fig. 2).

Step 1: Use the produced shorelines to remove the land area from the corresponding remote sensing images. This step is mandatory because the land area occupies a large area in each remote sensing image. When we analyze the statistical features of tidal flats, the presence of land area would largely influence the segmentation results.

Step 2: Divide the extracted tidal flats into multiple patches, based upon the natural spatial discontinuity of tidal flats' elements, five patches for our case, P1-P5 see Fig. 4. There are several benefits to do so. First, because of the extensive research area, the backscatter coefficient and NDWI values of each tidal flat element are influenced by different factors like ocean waves and the density of the suspended sediment. We need different segmentation parameters to best extract the morphological features of each tidal flat element. Division of the tidal flats can assure the accuracy of extracting the morphological feature of each tidal flat element. Second, the division improves the utilization of remote sensing images. Realizing that atmospheric situations and tidal dynamics are complex in our study area, we note that it is unlikely that all locations of an image are of a similar high quality. For instance, some parts of the area of interest in one optical image may be covered by clouds, while the rest are cloudless. Also, some areas of interest may have a high suspended sediment density, causing fuzzy edges of tidal flats and water, while other areas are not influenced by the suspended sediment. Third, splitting a large area into patches enhances the efficiency of statistical analysis.

Step 3: Use the multi-resolution segmentation method of Section 3.2.1 to identify the tidal flat pattern. For optical images, due to the large differences in NDWI-values between tidal flats and water, the pattern of tidal flats can be determined well. For SAR images, however, the backscatter coefficient is heavily influenced by the density of suspended sediment and soil moisture. Therefore, we introduce the texture parameter and a small scale parameter (e.g., 20) to distinguish tidal flats and water.

Step 4: Carry out post-processing to manually correct or remove the inaccurate segmentation results. The low quality of remote sensing images is a major reason for inaccurate segmentation results. For instance, considerable speckle noise, similar soil moisture, and the high

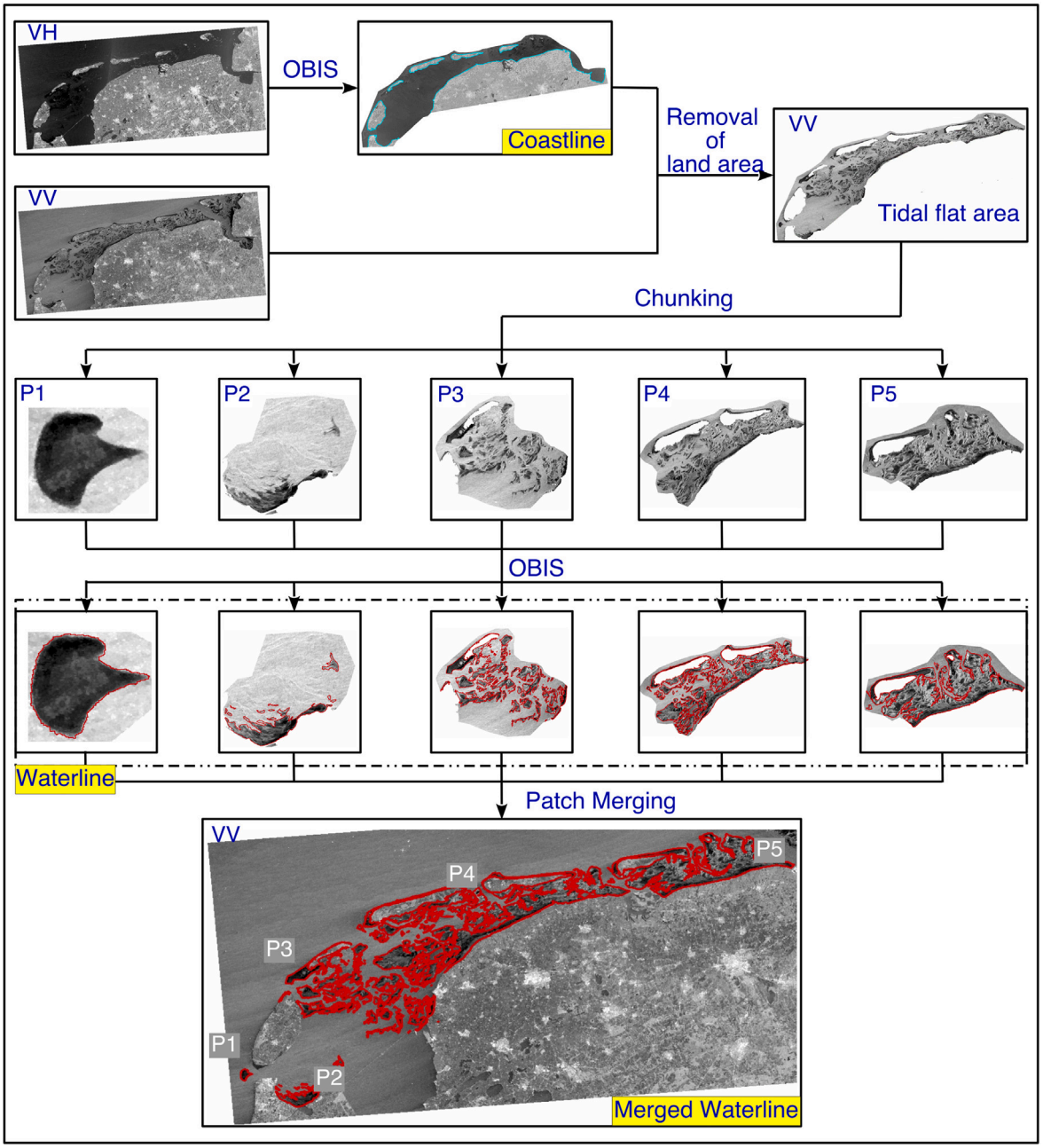

Fig. 4. The procedure of shoreline (in cyan) and waterline (in red) extraction from a SAR image example, acquired by Sentinel-1B satellite on 18 November 2017, described in Section 3.2. P1-P5 are the five different patches. (For interpretation of the references to color in this figure legend, the reader is referred to the web version of this article.)

density of suspended sediment in SAR images lead to unclear edges between tidal flats and water. Thanks to the enhanced image quality and reasonable segmentation parameters setting, manual intervention is minimal in this study. In case manual intervention is cumbersome when handling a large number of images, automatic post-processing methods are recommended, e.g., neural network architectures or histogram modification strategies (Zhang et al., 2021b).

Fig. 4 displays the procedure of shoreline and waterline extraction by OBIS from SAR imagery.

3.3. Water level simulation and assignment

After obtaining waterlines, the next step is to determine water level values for the waterlines extracted from remote sensing images (see Fig. 2).

3.3.1. Water level simulation

Due to tidal phase differences arising from tidal wave propagation, tidal deformation caused by the complex underwater terrain and the extensive study area (approximately 180 km in the West-East direction), an uneven spatial distribution of the instantaneous tidal level field occurs. We employed tidal models to hindcast the water level at the acquisition time of every remote sensing image, using a temporal sampling rate equal to the minute level. Two models are used in this study.

The Delft3D Flexible Mesh (DFM), numerical model that uses a shallow-water flow solver based on the finite volume method (Elias, 2006) and supports the use of triangular or rectangular grids for computation. It comprehensively considers the boundary conditions over the area of interest, meteorological forcing conditions (wind and pressure), bathymetry, and salinity to simulate the water level variation within the model domain (Nederhoff et al., 2021).

The TPXO (Oregon State University TOPEX/Poseidon Global Inverse Solution tidal model) global tide model (Egbert and Erofeeva, 2002) that obtains patches using consistent bathymetry and boundary conditions, and the same altimetry data sets for assimilation (Egbert et al., 1994). It can offer a 1/30 degree resolution fully global solution.

3.3.2. Water level assignment

The water level simulation results are first used to create a triangular irregular network and are then re-sampled to a 30 m grid to match the pixel spacing of remote sensing images. The extracted waterlines are discrete into points with a 30 m interval to facilitate overlaying with the corresponding water level simulation results. Lastly, the water height values derived from the water level simulation are assigned to the spatially nearest points.

3.4. Tidal flat DEM creation

The point clouds of waterlines with the assigned water height are used to interpolate a continuous DEM using Kriging (Oliver and Webster, 1990). Both Ordinary and Universal Kriging are recommended. The semivariogram models for Ordinary Kriging include the spherical, circular, Gaussian and Linear models, while for Universal Kriging, a linear and quadratic drift are recommended. Considering the pixel spacing of re-sampled remote sensing images and water level grid, we used a 30 m resolution. Kriging was used to interpolate values at every grid node. To obtain only the interpolation results of the area-of-interest (AOI), i.e., the full tidal flat area, we used a tidal flat outline to suppress extrapolation, i.e., to mask out irrelevant interpolation results. The outline is a waterline derived from a remote sensing image whose acquisition time was as close as possible to the moment of the lowest tide. The contour at a height of −1.6 m serves as a proxy, and additional analysis is conducted based upon this reference outline.

3.5. Morphological and topographic evolution analysis

The main components of the Dutch Wadden Sea on which we focus are the coastal tidal flat area from the inland and the islands, the sandbanks and tidal flats. Their annual features are analyzed, in terms of their morphological evolution, their topographic evolution and their volume change.

For tidal flats and coastal tidal flat area, we analyze their topographic evolution and volume changes. First, the topographic difference between the consecutive waterline-derived DEMs as defined in Section 3.4 is obtained. Then, the volume change equals

$$V = \sum_{k=1}^{N} (h_2(k) - h_1(k)) \cdot r^2, \tag{2}$$

where k indicates kth grid, N is the number of grid cells, h_1 and h_2 are the heights corresponding to the first and second DEMs, r indicates the grid size of DEM, and r^2 is the area of the square grid. A negative value indicates erosion, while a positive value represents deposition. The net volume change of the intertidal zone is obtained by the sum of erosion volume and deposition volume

$$V_{net} = V_{erosion} + V_{deposition}. \tag{3}$$

Sandbanks usually have rather irregular patterns, inhomogeneous substance distribution and potentially dramatic geomorphology changes. Therefore, we mainly analyze their shapes, areas and geometric centers (centroids) as being indicative of their movement direction. To quantify sandbank evolution, we first extract their boundaries from DEMs and track their geometric changes over time. We then analyze their migration patterns by computing the displacement of centroids over different time periods.

3.6. Accuracy validation

The extracted annual DEM time series was validated using external LiDAR and ground anchor measuring data. The high-frequency ground anchor measuring data was downsampled to one year matching the temporal resolution of the waterline-derived DEMs. The Mean Absolute Error (MAE) is calculated based on the following equation, being the validation indicator for the annual DEM.

$$MAE(t) = \frac{\sum_{1}^{K_{external}} |h^t_{external}(K_{external}) - h^t_{dem}(K_{dem})|}{n}, \tag{4}$$

where n is the number of external data, $K_{external}$ indicates Kth data from the external data, K_{dem} indicates the corresponding Kth grid from the waterline-derived DEM that is closest to Kth data from the external data, t indicates the specific year.

3.7. Uncertainty analysis

As potential main interference factors, the uncertainties of geocoding, waterline extraction, water level simulation, and interpolation can accumulate and affect the reliability of DEM. Therefore, their uncertainties should be evaluated, respectively.

3.7.1. Geocoding uncertainty

The geocoding accuracy of various datasets (see Section 3.1.1) has implications for the minimum level of shoreline change this method can detect, along with its spatial and temporal variability. To quantify the accuracy, the Root Mean Square Error (RMSE) of multiple Ground Control Points (GCPs) deviations are derived using the Haversine formula (Robusto, 1957) followed by converting these to the pixel level using the following equations:

$$RMSE_{geo} = \left(\sum_{q=1}^{p} \frac{2R \cdot \arcsin\left(\sqrt{\sin^2\left(\frac{lat_s^q - lat_m^q}{2}\right) + \cos(lat_m^q) \cdot \cos(lat_s^q) \cdot \sin^2\left(\frac{lon_s^q - lon_m^q}{2}\right)}\right)}{p}\right) / PXS, \tag{5}$$

where p is the number of GCPs, q is the qth GCP, R is the radius of the Earth ~6371 km, lat_m^q and lat_s^q are the latitudes of the qth GCP in master (m) and slave (s) images, lon_m^q and lon_s^q are the longitudes of the qth GCP in master and slave images, PXS is the pixel spacing (i.e., 30 m).

3.7.2. Waterline extraction uncertainty

Manually digitized waterlines serve as a reference for evaluating the spatial discrepancies of the extracted waterlines. Both datasets are initially discretized into scattered point sets. Subsequently, a representative subset of these points is selected to quantify deviations, which are then transformed from pixel-based measurements into physical distances.

$$RMSE_{extract} = \sqrt{\frac{1}{n}\sum_{i=1}^{n}(pix_{ref,i} - pix_{extract,i})^2} \cdot PXS, \tag{6}$$

where n is the number of reference points, q is the qth reference point, $pix_{ref,i}$ is the location of ith reference point, $pix_{extract,i}$ is the location of ith point from extracted waterline, PXS is the pixel spacing (i.e., 30 m).

3.7.3. Water level simulation uncertainty

Tidal observations from the measurement station are employed as validation data to assess the uncertainty of the tide model by comparing its simulated outputs with the observed tidal measurements. The uncertainty of the water level simulation is

$$RMSE_{simu} = \sqrt{\frac{1}{m}\sum_{j=1}^{m}(H_{model,j} - H_{ref,j})^2}, \tag{7}$$

where m is the number of reference points, j is the jth reference point, $H_{ref,i}$ is the measured tidal level, $H_{model,j}$ is the simulated tidal level by DFM or TPXO.

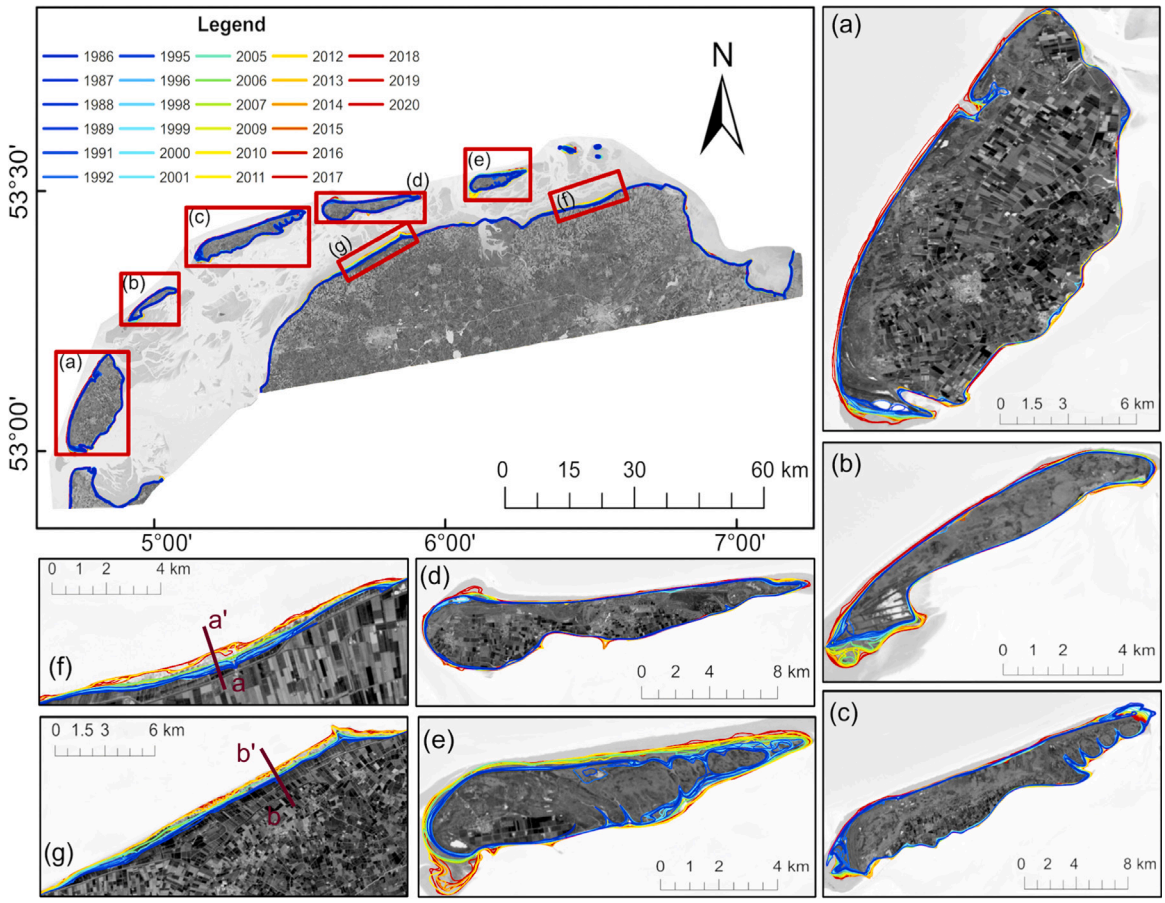

Fig. 5. Coastal tidal flat evolution from 1986 to 2020 superimposed on a Landsat −8 image captured on 20 July 2016. (a) Texel, (b) Vlieland, (c) Terschelling, (d) Ameland, (e) Schiermonnikoog, (f) Groningen coast and (g) Friesland coast. a-a′ and b-b′ are profiles used for displaying coastal tidal flat evolution (see Figs. 6(f)–(g)).

3.7.4. Interpolation uncertainty

The elevation data from 58 ground anchor stations is utilized to evaluate the uncertainty associated with a Kriging interpolation. Specifically, data from 50 stations is used as input for performing the Kriging interpolation, while the remaining 8 stations are reserved for validation. The uncertainty of the Kriging interpolation is quantified as follows

$$\mathrm{RMSE}_{\mathrm{interp}} = \sqrt{\frac{1}{u}\sum_{u=1}^{v}(\mathrm{Z}_{interp,u} - \mathrm{Z}_{ref,u})^2}, \tag{8}$$

where v is the number of reference points, u is the uth reference point, $\mathrm{Z}_{ref,i}$ is the reference point's height, $\mathrm{H}_{interp,j}$ is the interpolated height.

3.7.5. Total cumulative uncertainty

Assume systematic error (Bias) is negligible, then the relationship of RMSE and variance ($\mathrm{RMSE}^2 = \mathrm{Bias}^2 + \sigma^2$) could be simplified as $RMSE = \sigma$. The total cumulative uncertainty is

$$\sigma_{\mathrm{total}} = \sqrt{\sigma^2_{\mathrm{geo}} + \sigma^2_{\mathrm{extract}} + \sigma^2_{\mathrm{simu}} + \sigma^2_{\mathrm{interp}}}. \tag{9}$$

4. Results

4.1. Data pre-processing results

10 GCPs evenly distributed on the remote sensing images were selected to validate the geocoding accuracy between S1 GRD, RS-2 SLC, and Landsat. The result shows that their RMSE of deviations are less than 0.5 pixel. Based upon the method described in Section 3.1, the noisy/cloudy images and those images merely captured submerged tidal flats were excluded. The number of SAR and Landsat images used for shoreline estimation and DEM creation is separately listed in the third and sixth columns of Table 10 in Appendix B. 331 cross-polarization SAR images from 2011 to 2020 and 79 high-quality optical images from 1986 to 2020 were used for shoreline extraction, while 172 and 29 high-quality co-polarization SAR and optical images were used for waterline extraction from 2011 to 2020. From this table, we found that almost 50% of co-polarization SAR and optical images that have noise/cloud or with the submerged tidal flats were excluded.

4.2. Coastal tidal flat evolution

The costal tidal flat areas of five islands including inland generally showed an increasing trend over the past 34 years (see Fig. 6 and Table 11 in Appendix C). The expansion mainly happened in the southwest corner of Texel, Vlieland and Terschelling, the southwest and east corner of Ameland and the whole of Schiermonnikoog. The northeast corner of Terschelling suffered from significant erosion and the maximum erosion distance was approximately 820 m. The maximum and minimum areas of the five islands and the corresponding year are displayed in Table 2. We found that all islands except Ameland had a minimum area in 1992. This could be caused by the acquisition time of the only high-quality Landsat −5 image in 1992, which was at a relatively high tide. Their minimum areas separately were 149.030 km^2 for Texel in 1992, 15.612 km^2 for Vlieland in 1992, 66.991 km^2 for Terschelling in 1992, 49.175 km^2 for Ameland in 1987 and 21.947 km^2 for Schiermonnikoog in 1992. We found that most of the results had a minimum area in 1992. This could be caused by the incomplete tidal flat observations at a relatively high tide obtained by the high-quality Landsat −5 image in 1992. Otherwise, our result in 1992

Table 2
The maximum and minimum areas of Texel, Vlieland, Terschelling, Ameland and Schiermonnikoog and the corresponding year.

Item	Minimum		Maximum	
	Area (km^2)	Year	Area (km^2)	Year
Texel	149.030	1992	157.834	2017
Vlieland	15.612	1992	19.966	2018
Terschelling	66.991	1992	75.405	2018
Ameland	49.175	1987	54.215	2020
Schiermonnikoog	21.947	1992	33.489	2020

reflects the actual situation. Their maximum areas were 157.834 km^2 for Texel in 2017, 19.966 km^2 for Vlieland in 2018, 75.405 km^2 for Terschelling in 2018, 54.215 km^2 for Ameland in 2020 and 33.489 km^2 for Schiermonnikoog in 2020, respectively.

Two profiles vertical to the corresponding coast (a-a′ and b-b′ in Figs. 5(f)–(g)) were used to display the coastline evolution (see Figs. 6(f)–(g)). The Groningen and Friesland coastlines expanded separately from 1992 to 2013 and 2000 to 2011. The maximum expanded distance of the Groningen and Friesland coastlines was approximately 496 m in 2018 and 680 m in 2015, respectively. The potential reason probably is land reclamation or reclamation of fish ponds.

The area of Texel mainly expanded in its southwest corner and its area increased about 0.1799 km^2 yr^{-1}. Its minimum area was 149.030 km^2 in 1992, while the maximum area was 157.834 km^2 in 2017. The Vlieland also expanded its area in its southwest corner with the speed of 0.1074 km^2 yr^{-1}. Its minimum area was 15.612 km^2 in 1992, while the maximum area was 19.966 km^2 in 2018. The Terschelling suffered from erosion in its northeast corner while deposition in its southwest corner. Its area increased about 0.1511 km^2 yr^{-1}. The minimum area was 66.991 km^2 in 1992, while the maximum area was 75.405 km^2 in 2018. The area of Ameland increased about 0.1140 km^2 yr^{-1}. The minimum area was 49.175 km^2 in 1987, while the maximum area was 54.215 km^2 in 2020. The Schiermonnikoog had a significant increase in the area of the entire island with a rate of 0.3241 km^2 yr^{-1}. The minimum area was 21.947 km^2 in 1992, while the maximum area was 33.489 km^2 in 2020.

4.3. Sandbank evolution

The sandbank exhibited a complex evolutionary process in morphological change and movement of position. The evolutionary process of four sandbanks is displayed in Figs. 7(a)–(d) and their annual area change is shown in Fig. 8 and Table 11 in Appendix C. We used the centroids of the irregular sandbanks to describe their historical movement tracks, see the colored and dot-line arrow in Fig. 7.

Noorderhaaks evolved from an ellipse into a scallop sector (see Fig. 7(a)). Its area increased at 0.064 km^2 yr^{-1}. Its minimum area was 3.952 km^2 in 1991, while the maximum area was 7.516 km^2 in 2017. Its centroid moved about 461 m with 120 ° w.r.t. the North (clockwise) from 1986 to 1998. It, however, moved approximately 796 m in the opposite direction from 1998 to 2020.

Rottumerplaat consisted of a main sandbank in the middle, a small sandbank in the top left corner and a newly appeared sandbank in the top right corner (see Fig. 7(b)). The small sandbank was submerged after 1989, while the new sandbank appeared in 2012. The area of Rottumerplaat increased at 0.073 km^2 yr^{-1}. Its minimum area was 0.613 km^2 in 1992, while the maximum area was 3.371 km^2 in 2013. The centroid of the main sandbank moved about 475 m with 290 ° w.r.t. the North from 1986 to 1996, about 156 m with 45 ° w.r.t. the North from 1998 to 2006, about 175 m with 190 ° w.r.t. the North from 2007 to 2012 and about 233 m with 130 ° w.r.t. the North from 2013 to 2020. The centroid of the new sandbank moved about 738 m with 155 ° w.r.t. the North from 2012 to 2020. Based upon the movement trend of the main sandbank and new sandbank, we speculate that both will merge and be a larger sandbank.

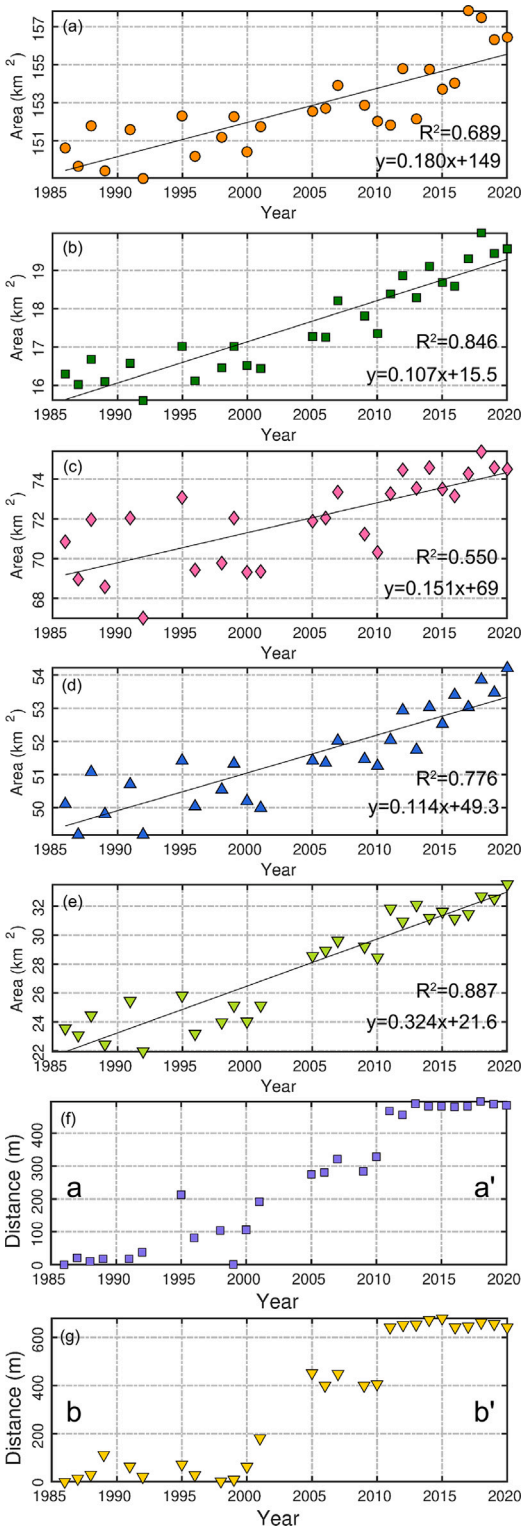

Fig. 6. The coastal tidal flat area/beach width change for the five islands and two coasts from 1986 to 2020: (a) Texel, (b) Vlieland, (c) Terschelling, (d) Ameland, (e) Schiermonnikoog, (f) Groningen coast and (g) Friesland coast. The locations of a-a′ and b-b′ profiles are marked on Figs. 5(f)–(g). The solid black lines in (a)–(e) show the best linear model of the area change over time and the coefficient of determination (shown at the bottom of each subfigure).

Table 3
The key parameter settings for the DFM model.

Parameter	Value
Time step	30 s
Water density	1023 kg m^{-3}
Bottom friction coefficient	Roughness map
Manning coefficient	$0.012 - 0.028$ s $m^{-\frac{1}{3}}$
Wind drag coefficient type	Charnock
Horizontal viscosity	0.1 m^2 s^{-1}

Rottumeroog initially eroded at the rate of 0.020 km^2 yr^{-1} from 1986 to 2001 and then expanded at 0.029 km^2 yr^{-1} from 2001 to 2020 (see Fig. 7(c)). Its minimum area was 0.284 km^2 in 2001, while the maximum area was 0.903 km^2 in 2013. It centroid moved about 171 m with 225 ° w.r.t. the North from 1986 to 1997, about 167 m with 90 ° w.r.t. the North from 1998 to 2008 and about 283 m with 165 ° w.r.t. the North from 2009 to 2020. Its movement trajectory looks like an infinity sign.

Zuiderduintjes experienced two evolutionary stages (see Fig. 7(d)). From 1986 to 2001, its centroid moved about 650 m with 120 ° w.r.t. the North. Its area, however, has barely changed. From 2005 to 2020, its position only moved about 210 m with 90 ° w.r.t. the North but its area had a fluctuating rising trend. Over the past 34 years, its area increased at 0.010 km^2 yr^{-1}, and its minimum and maximum areas were 0.071 km^2 in 1989 and 0.491 km^2 in 2006, respectively.

4.4. Intertidal DEMs

The quality of DEMs partly depends on the number of waterlines. We thus only concentrated on the data after 2011. Because of the insufficient waterlines in 2016, the DEM from 2015 to 2016 would be jointly produced. The other main factor influencing DEM quality is the water level simulation results. Based upon the accuracy of the created DEM using DFM and TPXO, the DFM performs better than TPXO (compared and discussed in Section 5.4). Specifically, the computational grid size using DEM was set up as 100 m for AOI. The gridded bathymetric data from the European Marine Observation and Data (EMODnet) and Dutch bathymetric data within the Rijkswaterstaat management area were combined to build the final bathymetry for the entire model domain. The meteorological forcing conditions used the ECMWF's ERA5 reanalysis dataset, which has a 0.25-degree (30 km) spatial resolution and hourly temporal resolution. The boundary conditions are specified at 305 different support points along AOI. Between these locations, the imposed values are linearly interpolated. The salinity of the Dutch Wadden Sea used an empirical value of 0.2 psu (practical salinity units). The key parameter settings for the model are summarized in the table below. Therefore, the DEMs displayed below were created using the DFM simulated water level results (see Table 3).

Using the method described in Sections Section 3.2.3, 3.3 and 3.4, the nine waterline-derived annual DEMs over the tidal flats in the Dutch Wadden Sea from 2011 to 2020 were created. The nine DEMs was separately extracted from the corresponding interpolation results using the same tidal flat outline, which was created manually based upon the SAR image acquired at the lowest tide (−1.59 m) during 2017. The areas of P2, P3, P4 and P5 equal 107.74 km^2, 359.70 km^2, 708.62 km^2 and 334.23 km^2, respectively.

Based upon the nine DEMs in Fig. 9, we found that the places near the islands and inland tend to have higher height values, such as Amsteldiep (P2), Groningen coast, and Friesland coast. Besides, the tidal flat area with relatively high elevation was clearly visible. And their patterns were relatively stable over time, such as the seven areas marked with the white squares shown in Fig. 9 for 2011. The detected maximum and minimum height values separately were 1.6 m and −1.6 m. Figs. 10 and 11 are the zoomed-in graphs to display further the tidal flat evolution details for P4 and P5, respectively.

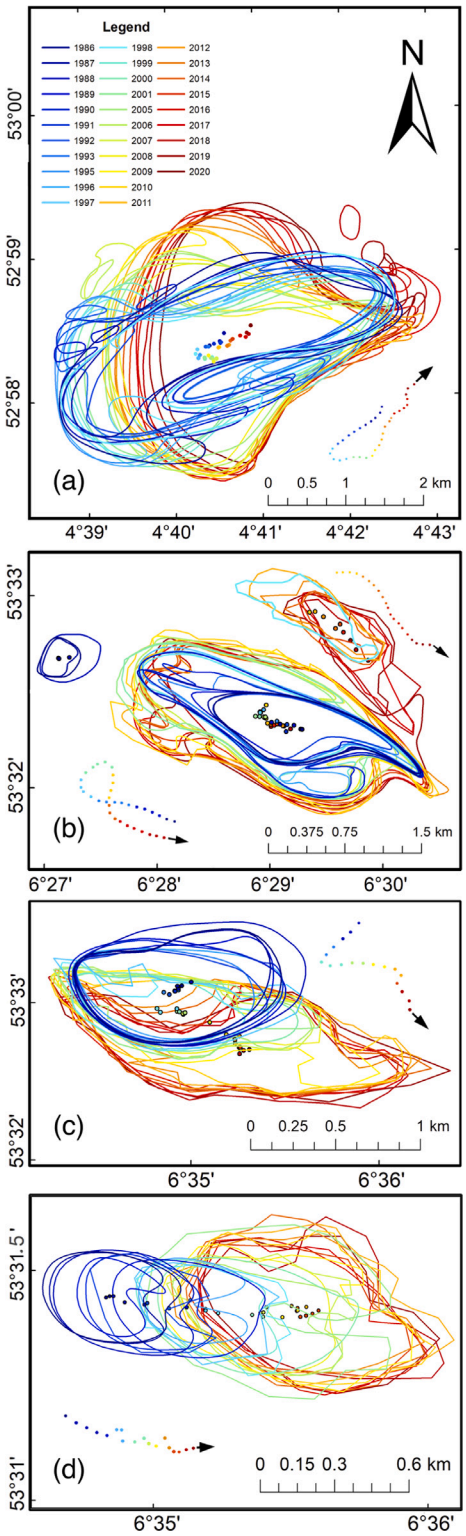

Fig. 7. Sandbank evolution from 1986 to 2020: (a) Noorderhaaks (P1), (b) Rottumerplaat, (c) Rottumeroog and (d) Zuiderduintjes. Their locations are displayed on Fig. 1(d). The dot indicates the centroid of the sandbank pattern. To avoid the overlap, the movement trend of sandbanks is shown with a colored dot-line arrow next to the sandbank outlines.

4.5. DEM validation

We separately selected three profiles from P4 (A-A′, B-B′ and C-C′) and P5 (D-D′ and E-E′ and F-F′) to further validate the accuracy of the waterline-derived DEM with four years of LiDAR data from 2016 to

Table 4
The MAE (mean absolute error) between the waterline-derived DEM and observations from 58 ground anchor measuring stations from 2011 to 2020. The unit is meter.

Year	2011	2012	2013	2014	2015–2016	2017	2018	2019	2020
Accuracy	0.183	0.187	0.255	0.257	0.170	0.169	0.199	0.178	0.202

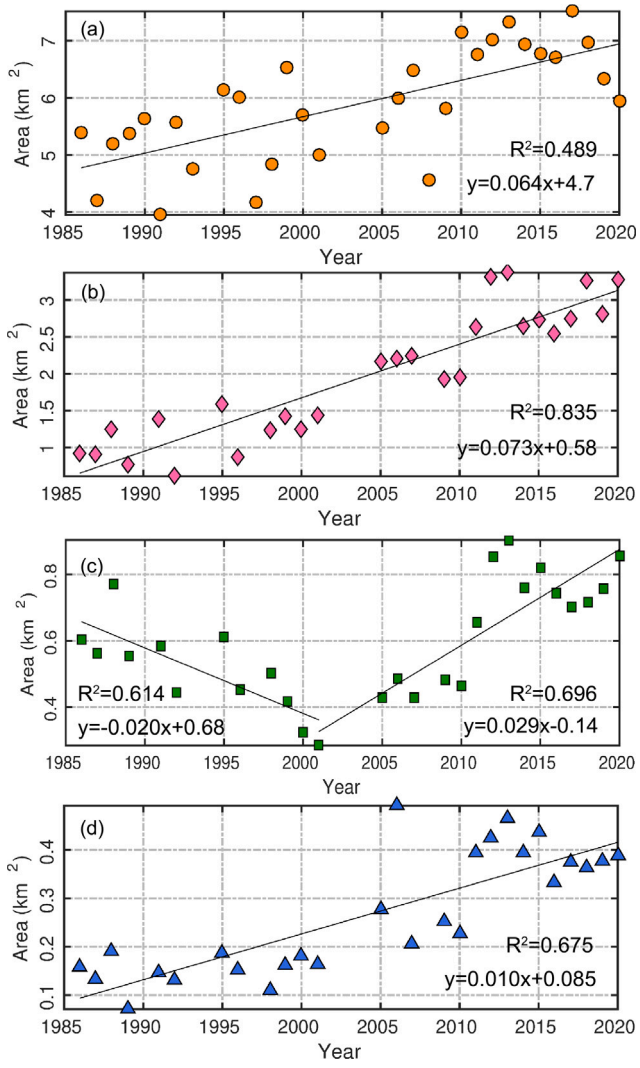

Fig. 8. The area change of four sandbanks from 1986 to 2020: (a) Noorderhaaks (P1), (b) Rottumerplaat, (c) Rottumeroog and (d) Zuiderduintjes. The solid black lines in (a)–(d) show the best linear model of the area change over time and the coefficient of determination (shown at the bottom of each subfigure).

2019. Fig. 12 compares the LiDAR- and waterline-derived DEM over six transects. A-A′, B-B′, C-C′ and D-D′ and E-E′ and F-F′ transects are covered by LiDAR data in 2016, 2017, 2018 and 2019, respectively. Therefore, we only compared their accuracy for the corresponding years, summarized in Table 5. C-C′ and D-D′ have a higher accuracy with MAE = 0.121 m and 0.189 m, respectively, while B-B′ and E-E′ have a relatively low accuracy with MAE = 0.332 m and 0.331 m, respectively. For F-F′ transect, there was a relatively high bias at 3-4 km, which is the location of Rottumerplaat. It is because part of Rottumerplaat is exposed to the Dutch Wadden sea all year round, similar to a small land. The waterline method, however, can only extract the intertidal DEM based upon waterlines and water level values.

Besides, we used 58 ground anchor measuring stations' data from 2011 to 2020 to validate the accuracy of the waterline-derived DEMs. In spatial domain, compared with the annual observations from the 58 ground anchor measuring stations (marked in Fig. 10 for 2011), the

Table 5
Mean absolute error (MAE) of six LiDAR- and waterline-derived topography profiles (A-A′, B-B′ and C-C′, and D-D′, E-E′ and F-F′ marked in Fig. 10 for 2019 and Fig. 11 for 2019, respectively). The unit is meter.

Year	A-A′	B-B′	C-C′	D-D′	E-E′	F-F′
2016	0.259					
2017		0.332				
2018			0.121	0.189		
2019					0.331	0.230

Table 6
The mean and standard deviation (std) of topographic difference of the intertidal zone in the Dutch Wadden Sea, including P2, P3, P4 and P5, from 2011 to 2020. The unit is meter.

Year	mean	std
2012–2011	−0.143	0.753
2013–2012	0.102	0.756
2014–2013	−0.120	0.830
2015/2016–2014	0.045	0.804
2017–2015/2016	−0.093	0.721
2018–2017	0.316	0.787
2019–2018	−0.178	0.812
2020–2019	0.165	0.900

accuracy of the nine DEMs was between 16.9 cm and 25.7 cm (see Table 4). We found that the DEMs have a higher accuracy in 2017–2020 than in 2011–2016. It could be caused by (1) more remote sensing images are available in 2017–2020 than in 2011–2016; or (2) S1A/B GRD data used in 2017–2020 has less noise than RS2 SLC used in 2011–2016. In the temporal domain, the statistical results of the 58 ground anchor measuring stations are displayed in Fig. 13. Except for S70, their mean errors are [−34, +13] cm and median errors are [−48, +6] cm.

4.6. Topographic and sedimentary evolution

To analyze and understand the topographic and sedimentary evolution of the intertidal zone in the Dutch Wadden Sea, its topographic difference maps (including P2, P3, P4 and P5) were generated in a daisy-chain manner (see Fig. 14). The positive values represent expansion, while the negative values mean erosion. Their statistical characteristics are summarized in Fig. 15 and Table 6. From Fig. 15, we see that the peak of the kernel density plot for every subfigure is near zero. Based on Table 6, the mean height of the intertidal zone experienced a fluctuating change with the maximum expansion (0.316 m) and erosion (0.178 m) in 2018–2017 and 2019–2018, respectively.

Combining the DEM difference maps and the grid size (30 m × 30 m) of the intertidal DEM, the volume change for every patch and the whole intertidal zone from 2011 to 2020 are summarized in Table 7. Similar to the trend of the elevation changes, the net volume also shows a similar fluctuating trend. For a single patch, P3 and P5 have similar area sizes (359.70 km^2 for P3 and 334.23 km^2 for P5), but P3 has a higher volume change of deposition and erosion than P5. It implies that the inlets near P3 have a higher water flow than that of P5. For the intertidal zone of Dutch Wadden Sea, the maximum expansion (3.01×10^8 m^3) occurs in 2018–2017, while the maximum erosion (2.56×10^8 m^3) occurs in 2014–2013. Overall, the intertidal zone expanded with 8.6×10^7 m^3 from 2011 to 2020. Elias et al. (2012) also demonstrated that sediment accumulation in the Dutch Wadden Sea exceeds the rate required to compensate for sea-level rise, indicating a net positive sedimentation

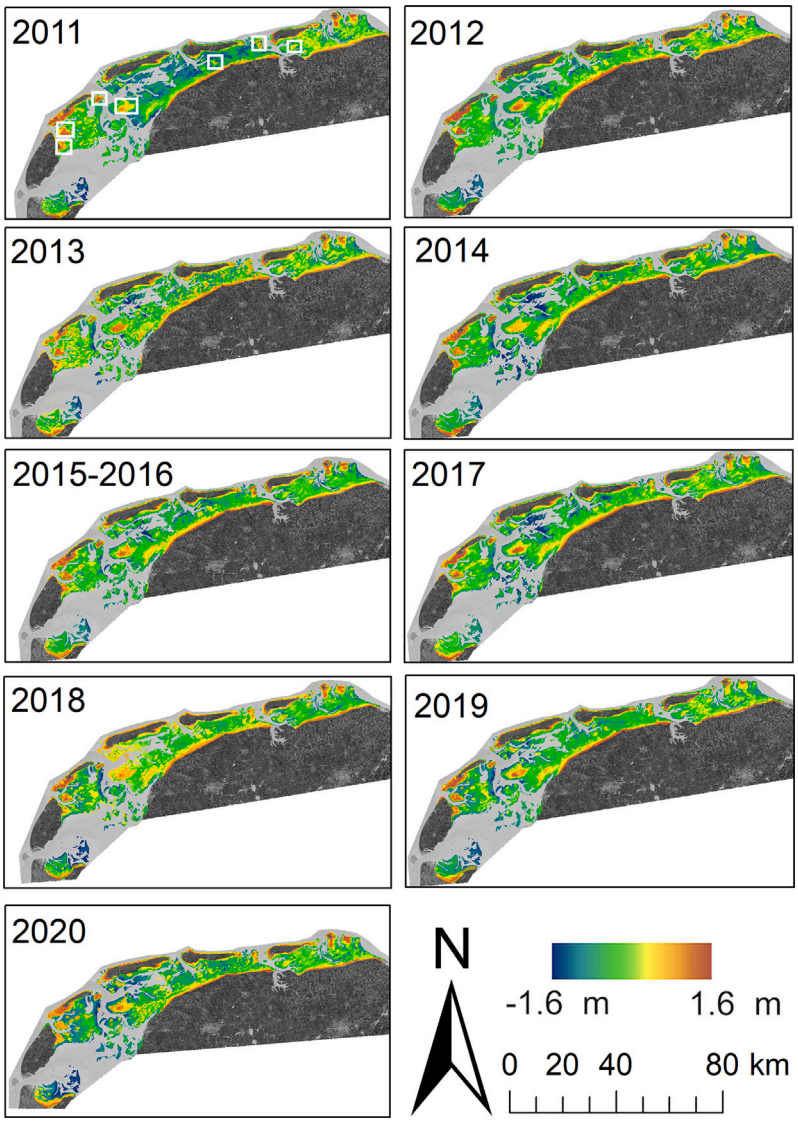

Fig. 9. Tidal flat DEM in the Dutch Wadden Sea from 2011 to 2020 superimposed on a Sentinel-1B image with VH polarization captured on 20 December 2020. The reference system is MSL (mean sea level). The white squares show seven parts whose morphological characteristics are significant.

Table 7
Volume change of the intertidal zone in the Dutch Wadden Sea from 2011 to 2020. P2, P3, P4 and P5 represent the patches displayed in Fig. 1(d).

Year	Erosion ($10^6 m^3$)				Deposition ($10^6 m^3$)				Total
	P2	P3	P4	P5	P2	P3	P4	P5	
2012–2011	−17	−71	−84	−21	1	8	70	51	−63
2013–2012	−2	−21	−69	−72	27	105	164	13	145
2014–2013	−24	−123	−173	−44	2	15	63	28	−256
2015/2016–2014	−3	−26	−104	−32	13	58	65	52	23
2017–2015/2016	−15	−61	−82	−35	2	20	60	26	−85
2018–2017	−1	−3	−26	−32	29	123	172	39	301
2019–2018	−30	−84	−149	−59	3	13	55	26	−225
2020–2019	−8	−15	−22	−14	13	64	160	68	246
Total	−100	−404	−709	−309	90	406	809	303	86

rate. This may be attributed to the fact that the beach area has a structure of a lagoon surrounded by five islands. Such a shape supports sediment deposition and is not subject to strong sea erosion forces.

To further display the area change of the study area and reduce the errors induced by the number of remote sensing images at low-tide, the statistical analysis was performed at four contours, i.e., -100 cm, -50 cm, 50 cm, and 100 cm. The Dutch Wadden Sea tidal flats has experienced a complex sedimentation process from 2011 to 2020 (see Fig. 16). This is evidenced by the inability of simple functional models (e.g., linear, exponential, or oscillatory functions) to adequately fit the observed data, except for higher-order functions (e.g., fourth-order polynomials). Compared with the areas above 100 cm and below -100 cm, the area between −50 cm and 50 cm has more complex sediment transport activities. Folmer et al. (2023) reached the same conclusion and contributed this performance to the associated shear is larger in the upper intertidal.

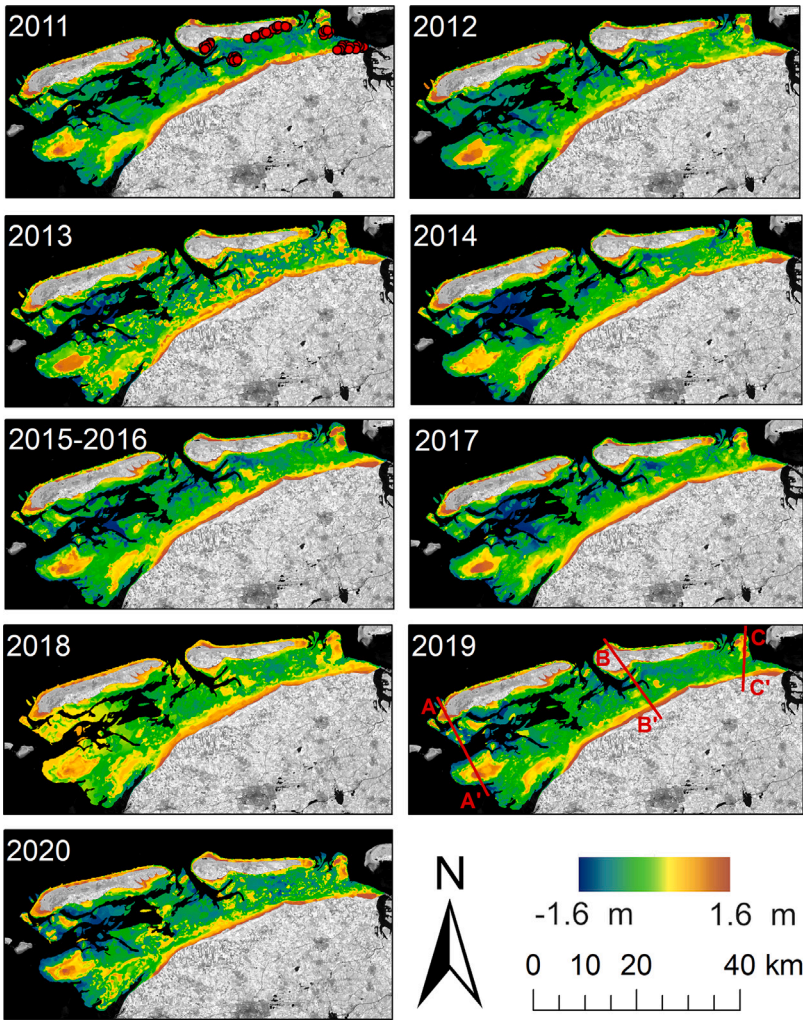

Fig. 10. Tidal flat dynamics of P4 patch from 2011 to 2020 superimposed on a Landsat −8 image captured on 20 July 2016. The orange indicates deposition, while the blue indicates erosion. The green indicates the stable area. The islands are Terschelling and Ameland from west to east, respectively. The reference system is MSL. The red dots represent the locations of 58 ground anchor measuring stations. A-A′, B-B′ and C-C′ are the profiles discussed in Section 4.5 and displayed in Fig. 12. (For interpretation of the references to color in this figure legend, the reader is referred to the web version of this article.)

5. Discussion

This section discusses the research significance and benefits and limitations of the generic scheme, the potential factors affecting the waterline extraction, water level simulation and the accuracy of DEM, and sketches the way forward.

5.1. Research significance and benefits and limitations of the generic scheme

For the Dutch Wadden Sea, numerous studies have delved into tidal dynamics between the North Sea and the Dutch Wadden Sea. They considered sediment composition, the mechanism between wind and flow, species change, hydrodynamics modeling and dike construction (Jordan et al., 2021; Folmer et al., 2023; van Weerdenburg et al., 2021; Beukema and Dekker, 2020; Gräwe et al., 2016; van Loon-Steensma et al., 2014). Few published studies, however, have focused on the Dutch Wadden Sea DEM, creating a notable gap in research. Our study addresses this gap by using a generic scheme that maximizes the potential of multi-source remote sensing imagery, including various imaging mechanisms and Object-Based Image Segmentation, to generate tidal flat DEMs. Using this scheme offers distinct advantages compared to previous studies. Kang et al. (2017) proposed a multiple-iteration method achieving an accuracy of 18.2 cm, while our method attains a better accuracy without the need for multiple iterations. We have achieved accuracies as high as 12 cm, surpassing the accuracy of 29 cm achieved by Zhang et al. (2022b) using deep learning methods. The generic scheme, however, has limitations that require further attention. For instance, limitations in remote sensing imagery result in the scheme's inability to capture tidal flat seasonal variations, potentially leading to interpretation errors in the annual DEM. Addressing these limitations is crucial for enhancing the reliability and applicability of our methodology.

5.2. Factors affecting the identification of waterlines

Waterline extraction is an important step for creating intertidal DEM. Three factors significantly affect its extraction accuracy. First, multiple environmental factors, e.g., currents, waves, and underwater topography, influence the sea surface roughness. This is well visible from remote sensing images, especially SAR images, and causes an unclear edge between tidal flats and water. Second, the presence of moisture in sandy sediments causes difficulty in distinguishing tidal flats from water. Third, the irregular shape of tidal flats is challenging for

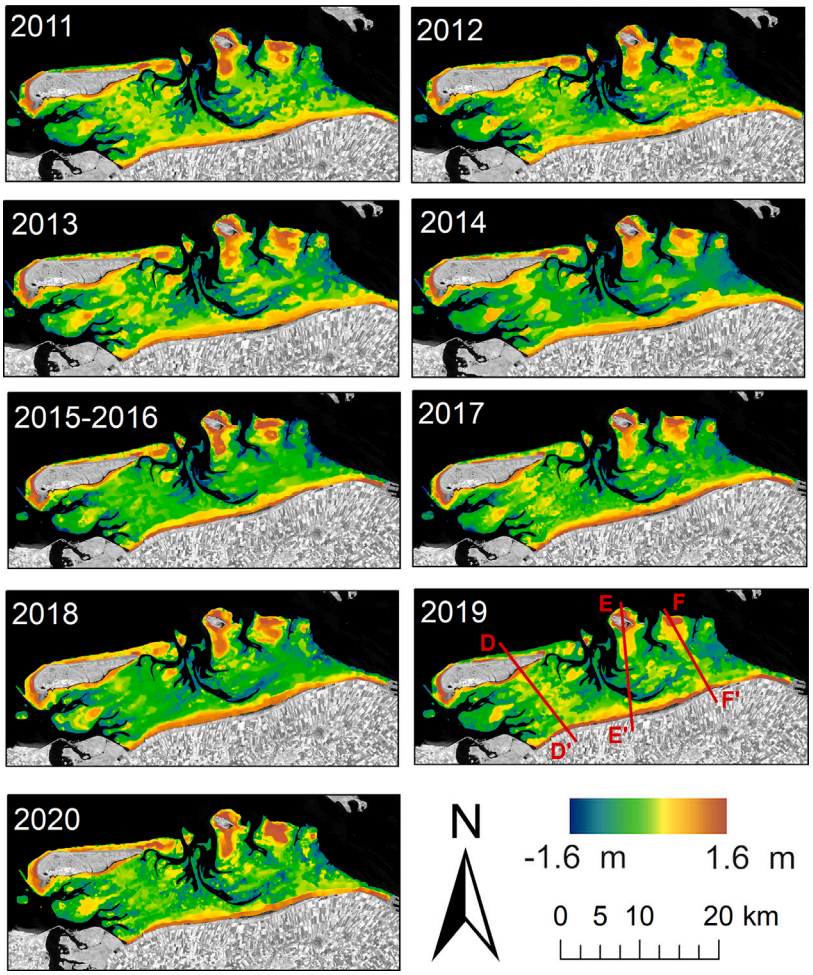

Fig. 11. Tidal flat dynamics of P5 patch from 2011 to 2020 superimposed on a Landsat −8 image captured on 20 July 2016. The orange indicates deposition, while the blue indicates erosion. The green indicates the stable area. The island is Schiermonnikoog. The reference system is MSL. D-D′, E-E′ and F-F′ are the profiles discussed in Section 4.5 and displayed in Fig. 12. (For interpretation of the references to color in this figure legend, the reader is referred to the web version of this article.)

waterline extraction and no unique parameter suits all waterline extraction cases. This can be corrected by post-processing. For instance, manual removal of inappropriate segmentation results or re-conducting segmentation for low-quality images using other segmentation parameters may be suited.

5.3. Factors affecting the accuracy of water level simulation

Water level simulation results are important in creating a high-accuracy intertidal DEM. The prediction accuracy of the water level, however, is influenced by factors, like the mesh resolution, bathymetric and meteorological data. For instance, the mesh resolution of DFM in the area of interest is around 300 m, while that of TPXO reaches 3700 m. The higher spatial resolution mesh can obtain a more detailed spatial representation of the water level. In addition, more recent bathymetric data could capture the bed level information more correctly due to morphological changes, and improve the hydrodynamic prediction of the model. As model inputs, the spatial and temporal resolution of meteorological data is important for the model to best simulate the instantaneous water level. In this study, we have taken the data as they are publicly available, but more targeted observations could improve the results.

5.4. Factors affecting the accuracy of DEM

We identified four factors that influence the accuracy of waterline-derived DEM.

(1) The temporal resolution of waterlines. More waterlines acquired at different times result into more details of the tidal flats. The ideal scenario is that the acquisition time of remote sensing images covers the entire tidal cycle, ensuring that the extracted waterlines cover the whole tidal flats.

(2) The spatial resolution of remote sensing images. In contrast to the comparatively low-spatial-resolution remote sensing images obtained from Landsat −5/7/8, newer satellites such as Sentinel-1A/B and Radarsat −2 offer data with significantly higher spatial resolution. This enhanced resolution enables them to capture and record more intricate details of the tidal flats with greater precision and clarity cf. Table 1.

(3) The accuracy of waterline extraction. Inaccurate waterline extraction results reflected in the remote sensing images are represented as pixel deviations. Hence, a poor segmentation result would lead to integer pixel size deviation, e.g., $n \times 30$ m ($n \geq 1$) for our case.

(4) The accuracy of water level simulation. To quantitatively estimate the influence of water level simulation results with different accuracy for the accuracy of the created DEMs, we used the same waterlines, different results of water level simulation from DFM and TPXO and the same interpolation method. The mean absolute error significantly increased using TPXO outputs (see Table 8), compared

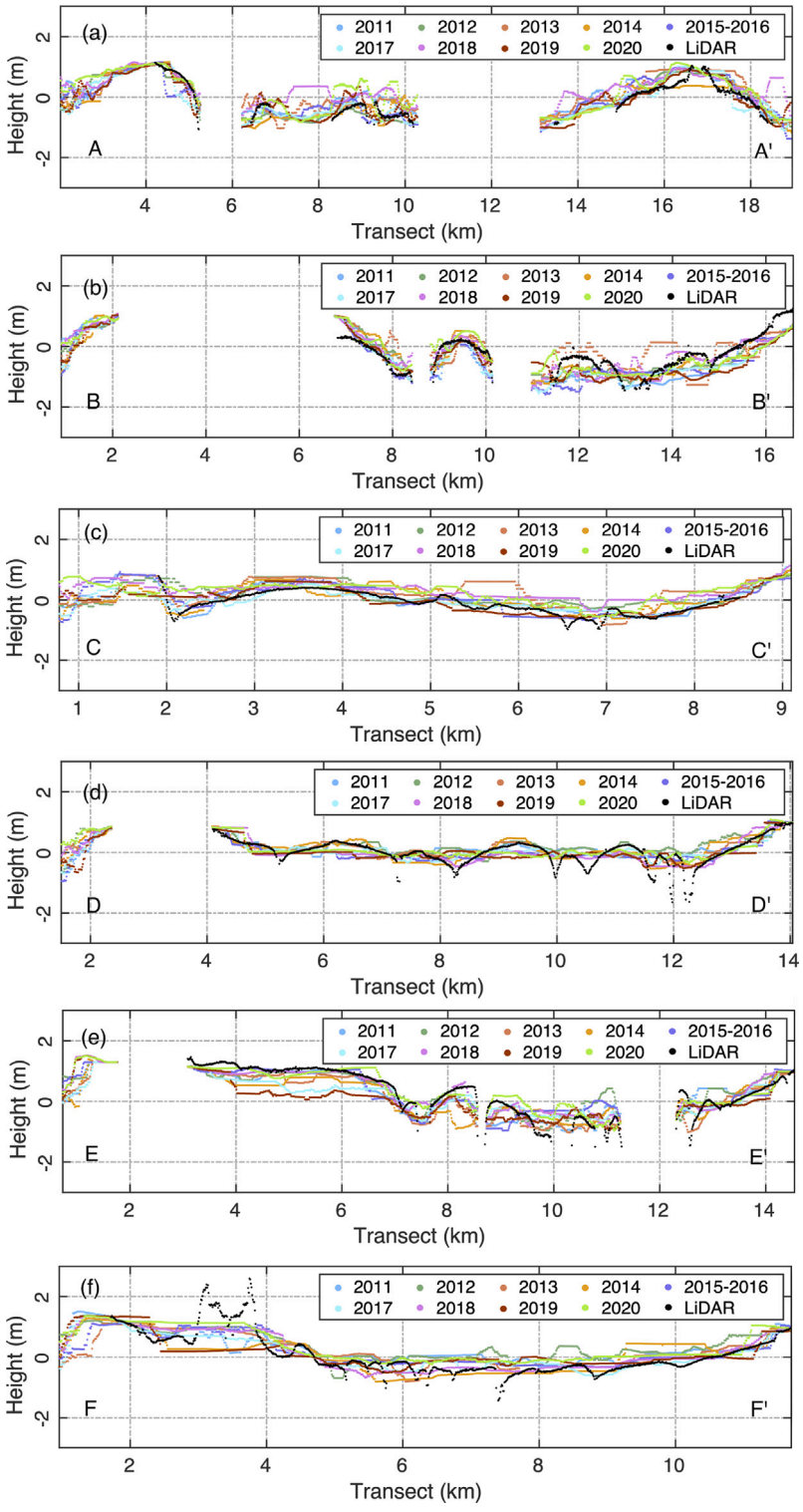

Fig. 12. (a) A-A′ and (b) B-B′ profiles from P4 are separately validated by LiDAR data from 2016 and 2017 marked in Fig. 10 for 2019. (c) C-C′ and (d) D-D′ profiles from P4 and P5 are validated by LiDAR data from 2018 and marked in Fig. 10 for 2019 and Fig. 11 for 2019, respectively. (e) E-E′ and (f) F-F′ profiles from P5 are validated by LiDAR data from 2019 and marked in Fig. 11 for 2019.

with DFM, demonstrating that DFM is more appropriate than TPXO for water level simulation in the Dutch Wadden Sea.

5.5. Uncertainty quantification

The geocoding uncertainty, as described in Section 4.1, is estimated to be approximately 15 m. A total of 20 waterlines were digitized into scattered point sets, from which 50 points were selected to assess the uncertainty associated with waterline extraction, yielding an uncertainty of approximately 30 m. The uncertainty in water level simulation, when compared with tidal gauge data, is approximately 0.2 m. The interpolation uncertainty is estimated to be about 0.5 m, as detailed in Section 3.7.5. According to Eq. (9), the total cumulative uncertainty is approximately 33.55 m. Among the four sources of

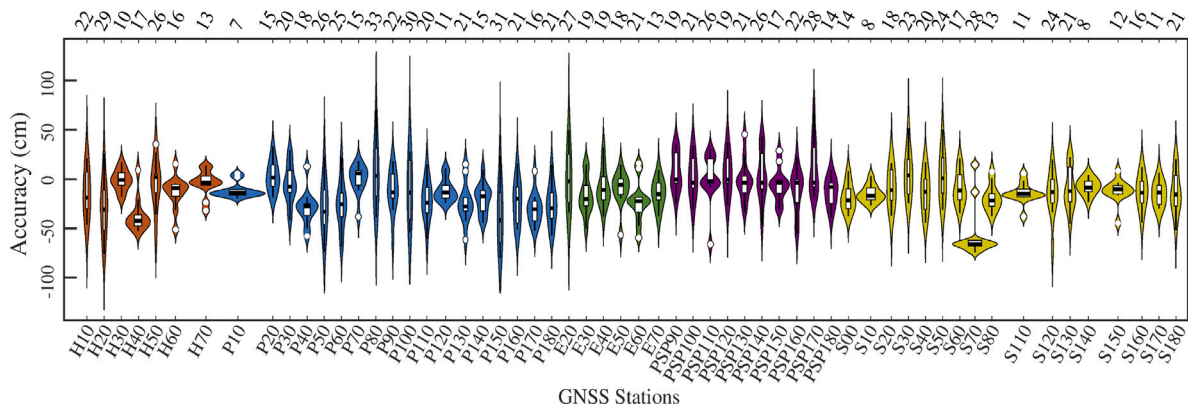

Fig. 13. Violin plots of the errors between the waterline-derived DEM and observations from 58 ground anchor measuring stations from 2011 to 2020. The locations of 58 ground anchor measuring stations are marked in Fig. 1(d). Each violin plot includes a box plot and a kernel density plot. The horizontal black line indicates the median, while the box indicates the interquartile range of the values. The vertical black line is the upper and lower limits of the values after removing outliers. The white dots indicate the outliers. The width of the violin in each subfigure is scaled by the number of samples. The numbers at the top of the image represent the standard deviation of the errors between the waterline-derived DEM and observations (their units are centimeters).

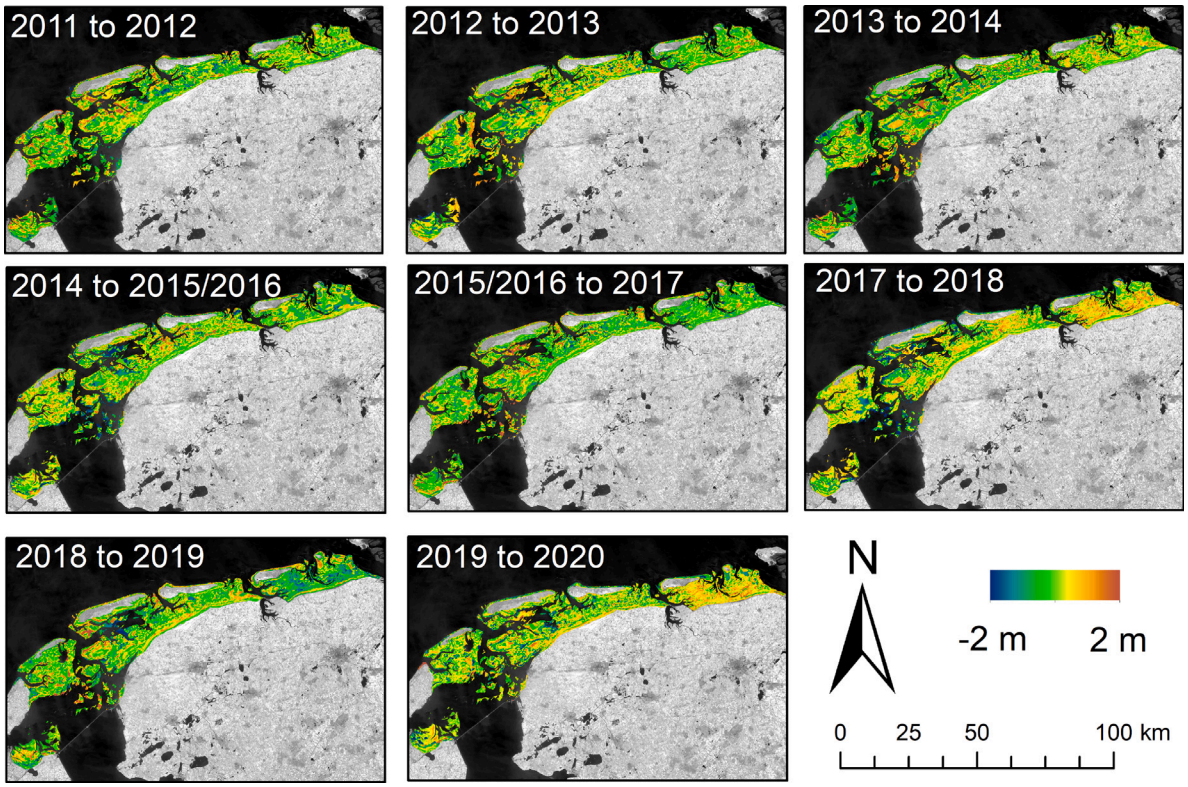

Fig. 14. Topographic difference maps of the intertidal zone in the Dutch Wadden Sea from 2011 to 2020 superimposed on a Landsat −8 image captured on 20 July 2016. The red indicates deposition, while the blue indicates erosion. The green indicates the stable area. The reference system is MSL (mean sea level). (For interpretation of the references to color in this figure legend, the reader is referred to the web version of this article.)

Table 8
The MAE (mean absolute error) between the waterline-derived DEM using water level results from DFM and TPXO and observations from 58 ground anchor measuring stations. The unit is meter.

Year	2017	2018	2019	2020
DFM	0.169	0.199	0.178	0.202
TPXO	0.576	0.338	0.533	0.363

uncertainty, the primary contributors to overall uncertainty were the variability in waterline extraction and geocoding errors, both of which had the most significant impact on vertical elevation estimates.

5.6. The role of sandbanks in tidal flat evolution

The observed changes in sandbanks (as shown in Section 4.3), particularly their migration and expansion, suggest significant interactions with tidal flat dynamics. The migration patterns of these sandbanks indicate shifts in tidal currents, which could influence sediment deposition and erosion processes on tidal flats. The growth of Noorderhaaks, for instance, likely contributed to the sediment supply of nearby tidal flats, enhancing their stability. Conversely, the erosion of Rottumeroog sandbank may have increased sediment loss in adjacent intertidal zones. Without sufficient sediment input, tidal flats may become more vulnerable to erosion and sea-level rise impacts. Future

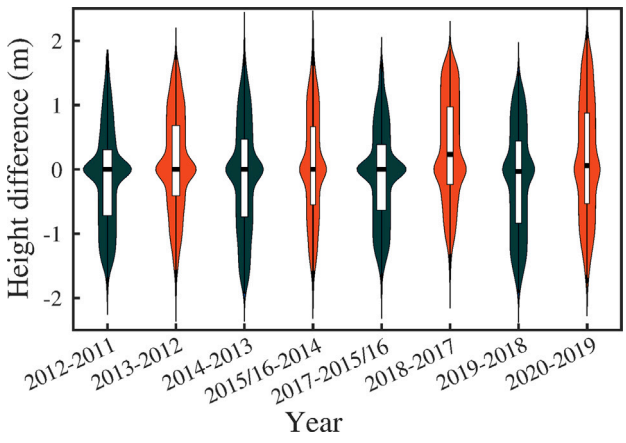

Fig. 15. Violin plots of the topographic difference maps of the intertidal zone in the Dutch Wadden Sea. Each violin plot includes a box plot and a kernel density plot.

research should integrate hydrodynamic modeling with remote sensing observations to quantify sediment exchanges between sandbanks and tidal flats, improving predictions of coastal landscape evolution under changing environmental conditions.

5.7. The way forward

Our scheme is generic and suits tidal flat dynamic mapping based upon remote sensing images. The standard data pre-processing step is suitable for all SAR data formats (including GRD and SLC) and optical data formats and is fully automated once parameters are pre-configured. Our proposed method of selecting high-quality SAR images based upon polarimetric features enhances efficiency. The shoreline and waterline extraction method based upon the OBIS and dual-polarization SAR data results into a convenient way of operation and into a solid visual interpretation. The removal of the land boundaries and partition processing steps improve the accuracy of local statistical analysis. The water level simulation model, i.e., TPXO and DFM (https://oss.deltares.nl/web/delft3dfm), is freely accessible and DFM provides the corresponding Wadden sea model. The interpolation method is also available from different geoanalysis software packages.

The waterline extraction based upon the OBIS can as yet not be batch processed. At times, further post-processing is necessary to enhance the accuracy of automatically extracted waterlines. Besides, due to the complex tidal environment (e.g., the suspended sediment), edges between the tidal flats and water in co-polarization SAR images are vague, which easily causes segmentation errors. To address this, post-processing needs to be implemented. Although the DFM performs better than TPXO, additional work, e.g., to get the DFM model, is required to simulate the water level in a particular period. The water level assignment for each waterline needs to be implemented individually. Because of the inherent drawbacks of the waterline method, the generic scheme particularly suits the intertidal zones.

The increasing number of satellites and drones can provide increasingly many remote sensing data. Therefore, we are more likely to observe the entire tidal cycle, improving the accuracy of the created annual DEM. Meanwhile, obtaining a monthly or weekly DEM will be possible in the near future. And with the availability of high-resolution remote sensing data, the created DEMs will have a higher high-resolution, e.g., 3 m for TerraSAR-X with stripmap mode or 0.5 m for WorldView-2.

6. Conclusion

In this study, we designed and demonstrated a generic scheme using OBIS and polarimetric features of SAR data that combines radar and optical images to map almost four decadal Dutch coastal dynamics. We conclude that (1) the OBIS method well identifies the shorelines and waterlines from dual-polarization SAR data and optical data; (2) the removal of the land boundaries and partition processing steps are useful for improving the accuracy and efficiency of OBIS; (3) our scheme offers a comparable DEM product (12.1 cm accuracy) with respect to traditional techniques such as LiDAR, hence being an economical and efficient tool. Using this generic scheme and multi-source remote sensing data to map the tidal flat dynamics worldwide is an interesting challenge for future research.

CRediT authorship contribution statement

Bin Zhang: Writing – review & editing, Writing – original draft, Visualization, Validation, Software, Resources, Methodology, Investigation, Formal analysis, Data curation, Conceptualization. **Ling Chang:** Writing – review & editing, Supervision, Software, Resources, Methodology, Investigation. **Zhengbing Wang:** Writing – review & editing, Software, Resources, Methodology. **Li Wang:** Writing – review & editing, Validation, Software, Resources, Methodology, Conceptualization. **Qinghua Ye:** Writing – review & editing, Software. **Alfred Stein:** Writing – review & editing, Validation, Supervision, Resources, Methodology, Investigation, Formal analysis.

Declaration of competing interest

The authors declare that they have no known competing financial interests or personal relationships that could have appeared to influence the work reported in this paper.

Acknowledgments

We thank the European Space Agency (ESA) for offering Sentinel-1A/B data, the Netherlands Space Office (NSO) for offering Radarsat −2 data and the United States Geological Survey (USGS) for offering Landsat data. We thank Dr. Erwin Bruinewoud and Ecologist Mr. Johan Krol from the Nederlandse Aardolie Maatschappij (NAM) for offering ground anchor measuring validation data. We thank Rijkswaterstaat (https://www.rijkswaterstaat.nl/) for offering LiDAR data and tidal gauge data. We thank Dr. Edwin Elias and Mr. Denzel Harlequin from Deltares for offering the Wadden Sea DFM model and Dr. Jord Warmink and Dr. Weiqiu Chen from University of Twente for supporting DFM installation. We thank Prof. Daphne van der Wal from University of Twente for discussing about water level simulation. We thank Nationaal Georegister (https://www.nationaalgeoregister.nl) and Dr. Julia A. Busch from the Wadden Sea world heritage for offering intertidal area data.

This research was funded by the Natural Science Foundation of Shanxi Province, China (Grant No. 202403021211007).

Appendix A. Information of remote sensing images summarized by acquisition year and missions

See Table 9.

Appendix B. Summary of the number of remote sensing images available, excluded, and high-quality by year

See Table 10.

Appendix C. The area evolution of the five islands and four sandbanks from 1986 to 2020

See Table 11.

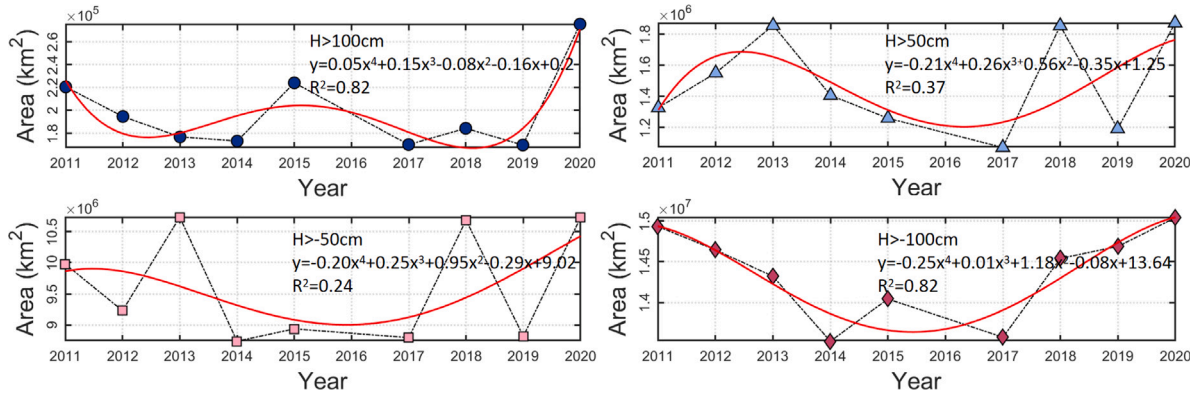

Fig. 16. Based upon area observations in 2011, the summed area changes and trends of P2, P3, P4 and P5 at four heights (–100 cm, -50 cm, 50 cm, and 100 cm) from 2011 to 2020 are shown. The solid red lines in (a)–(d) show the best linear model of the area change over time with the coefficient of determination at the top right corner of each subfigure. (For interpretation of the references to color in this figure legend, the reader is referred to the web version of this article.)

Table 9
Summary of remote sensing images used for this study by year and missions. L5, L7, L8, RS2(T202), RS2(T302), S1A and S1B separately indicate Landsat-5 TM, Landsat-7 ETM+, Landsat-8 OLI, Radarsat-2 in Track 202, Radarsat-2 in Track 302, Sentinel-1A and Sentinel-1B. '-' indicates that no image is available.

Year	Missions							
	L5	L7	L8	RS2(T202)	RS2(T302)	S1A	S1B	Total
1986	5	–	–	–	–	–	–	5
1987	3	–	–	–	–	–	–	3
1988	4	–	–	–	–	–	–	4
1989	2	–	–	–	–	–	–	2
1990	3	–	–	–	–	–	–	3
1991	2	–	–	–	–	–	–	2
1992	5	–	–	–	–	–	–	5
1993	3	–	–	–	–	–	–	3
1994	2	–	–	–	–	–	–	2
1995	7	–	–	–	–	–	–	7
1996	1	–	–	–	–	–	–	1
1997	3	–	–	–	–	–	–	3
1998	3	–	–	–	–	–	–	3
1999	5	4	–	–	–	–	–	9
2000	2	2	–	–	–	–	–	4
2001	2	1	–	–	–	–	–	3
2002	3	2	–	–	–	–	–	5
2003	–	–	–	–	–	–	–	–
2004	2	–	–	–	–	–	–	2
2005	3	4	–	–	–	–	–	7
2006	3	2	–	–	–	–	–	5
2007	–	5	–	–	–	–	–	5
2008	2	1	–	–	–	–	–	3
2009	2	2	–	–	–	–	–	4
2010	4	–	–	–	–	–	–	4
2011	3	2	–	12	14	–	–	31
2012	–	1	–	14	15	–	–	30
2013	–	3	–	16	15	–	–	34
2014	–	3	3	13	12	–	–	31
2015	–	4	5	15	6	–	–	30
2016	–	3	4	–	–	3	–	10
2017	–	3	3	–	–	19	17	42
2018	–	5	7	–	–	29	25	66
2019	–	4	3	–	–	31	30	68
2020	–	3	4	–	–	30	15	52
Total	74	54	29	70	62	112	87	488

Table 10
The number of remote sensing images available, excluded, and high-quality. L5, L7, L8, RS2(T202), RS2(T302), S1A and S1B separately indicate Landsat-5 TM, Landsat-7 ETM+, Landsat-8 OLI, Radarsat-2 in Track 202, Radarsat-2 in Track 302, Sentinel-1A and Sentinel-1B.

Year	Available missions	Nr. of available images	Nr. of excluded images		Nr. of high-quality images
			Noisy/cloudy images	Submerged tidal flat area	
1986	L5	5	1	1	3
1987	L5	3	2	0	1
1988	L5	4	2	1	1
1989	L5	2	0	0	2
1990	L5	3	2	0	1
1991	L5	2	0	0	2
1992	L5	5	4	0	1
1993	L5	3	1	0	2
1994	L5	2	2	0	0
1995	L5	7	4	0	3
1996	L5	1	0	0	1
1997	L5	3	1	1	1
1998	L5	3	2	0	1
1999	L5	5	1	0	7
	L7	4	1	0	
2000	L5	2	1	1	1
	L7	2	1	0	
2001	L5	2	0	1	1
	L7	1	0	1	
2002	L5	3	3	0	0
	L7	2	2	0	
2004	L5	2	2	0	0
2005	L5	3	0	0	5
	L7	4	2	0	
2006	L5	3	0	1	4
	L7	2	0	0	
2007	L7	5	1	0	4
2008	L5	2	0	1	1
	L7	1	1	0	
2009	L5	2	0	0	4
	L7	2	0	0	
2010	L5	4	0	0	4
2011	L5	3	1	0	16
	L7	2	1	0	
	RS2(T202)	12	2	4	
	RS2(T302)	14	2	5	
2012	L7	1	1	0	15
	RS2(T202)	14	3	5	
	RS2(T302)	15	2	4	
2013	L7	3	1	0	19
	RS2(T202)	16	2	8	
	RS2(T302)	15	1	3	
2014	L7	3	1	1	17
	L8	3	1	0	
	RS2(T202)	13	3	3	
	RS2(T302)	12	3	2	
2015	L7	4	3	0	13
	L8	5	2	1	
	RS2(T202)	15	3	6	
	RS2(T302)	6	1	1	
2016	L7	3	1	1	4
	L8	4	1	1	
	S1A	3	2	0	
2017	L7	3	1	0	22
	L8	3	1	0	
	S1A	19	2	7	
	S1B	17	3	6	
2018	L7	5	2	1	32
	L8	7	3	1	
	S1A	29	6	7	
	S1B	25	10	3	

(*continued on next page*)

Table 10 (*continued*).

Year	Available missions	Nr. of available images	Nr. of excluded images		Nr. of high-quality images
			Noisy/cloudy images	Submerged tidal flat area	
2019	L7	4	1	0	34
	L8	3	3	0	
	S1A	31	8	8	
	S1B	30	10	4	
2020	L7	3	2	0	26
	L8	4	1	1	
	S1A	30	5	9	
	S1B	15	1	7	

Table 11
The area evolution of the five islands (Texel, Vlieland, Terschelling, Ameland and Schiermonnikoog) and four sandbanks (Noorderhaaks (P1), Rottumerplaat, Rottumeroog and Zuiderduintjes) from 1986 to 2020. '-' indicates there is no data available.

Year	Area (km^2)								
	Texel	Vlieland	Terschelling	Ameland	Schiermonnikoog	Noorderhaaks	Rottumerplaat	Rottumeroog	Zuiderduintjes
1986	150.632	16.307	70.870	50.098	23.579	5.390	0.918	0.604	0.159
1987	149.652	16.011	68.955	49.175	23.058	4.212	0.909	0.561	0.134
1988	151.803	16.671	71.959	51.075	24.462	5.199	1.260	0.771	0.191
1989	149.398	16.093	68.581	49.799	22.444	5.377	0.772	0.555	0.071
1990	–	–	–	–	–	5.632	–	–	–
1991	151.565	16.582	72.030	50.716	25.468	3.952	1.39	0.583	0.146
1992	149.030	15.612	66.991	49.189	21.947	5.567	0.613	0.445	0.131
1993	–	–	–	–	–	4.765	–	–	–
1995	152.302	17.005	73.092	51.425	25.821	6.138	1.588	0.612	0.187
1996	150.156	16.114	69.412	50.040	23.194	6.010	0.870	0.453	0.153
1997	–	–	–	–	–	4.166	–	–	–
1998	151.169	16.463	69.778	50.548	23.962	4.838	1.237	0.501	0.110
1999	152.246	17.008	72.027	51.331	25.139	6.533	1.430	0.416	0.162
2000	150.409	16.524	69.319	50.205	24.051	5.698	1.250	0.322	0.182
2001	151.730	16.440	69.370	50.002	25.149	5.089	1.441	0.284	0.165
2005	152.534	17.271	71.892	51.412	25.578	5.473	2.165	0.427	0.277
2006	152.700	17.260	72.053	51.348	28.924	5.989	2.208	0.484	0.491
2007	153.908	18.202	73.366	52.021	29.621	6.476	2.247	0.428	0.206
2008	–	–	–	–	–	4.557	–	–	–
2009	152.867	17.812	71.234	51.458	29.174	5.816	1.929	0.481	0.252
2010	152.008	17.344	70.296	51.264	28.481	7.144	1.959	0.462	0.227
2011	151.815	18.383	73.256	52.035	31.821	6.754	2.639	0.656	0.394
2012	154.811	18.862	74.481	52.943	30.944	7.028	3.312	0.852	0.425
2013	152.141	18.294	73.526	51.744	32.115	7.336	3.371	0.903	0.466
2014	154.764	19.101	74.586	53.026	31.196	6.945	2.644	0.759	0.394
2015	153.725	18.683	73.499	52.519	31.638	6.783	2.731	0.820	0.437
2016	154.039	18.576	73.150	53.389	31.127	6.705	2.546	0.744	0.333
2017	157.834	19.297	74.268	53.036	31.475	7.516	2.746	0.703	0.375
2018	157.491	19.966	75.405	53.852	32.673	6.974	3.263	0.716	0.363
2019	156.313	19.446	74.566	53.458	32.532	6.341	2.806	0.756	0.376
2020	156.433	19.560	74.496	54.215	33.489	5.953	3.279	0.855	0.388

Data availability

The authors do not have permission to share data.

References

Alonso, A.C., Van Maren, D., Elias, E., Holthuijsen, S., Wang, Z., 2021. The contribution of sand and mud to infilling of tidal basins in response to a closure dam. Mar. Geol. 439, 106544.

Arens, S.M., Mulder, J.P., Slings, Q.L., Geelen, L.H., Damsma, P., 2013. Dynamic dune management, integrating objectives of nature development and coastal safety: Examples from the Netherlands. Geomorphol. 199, 205–213.

Asare, Y.M., Forkuo, E.K., Forkuor, G., Thiel, M., 2020. Evaluation of gap-filling methods for Landsat 7 ETM+ SLC-off image for LULC classification in a heterogeneous landscape of West Africa. Int. J. Remote. Sens. 41 (7), 2544–2564.

Baatz, M., 2000. Multi resolution segmentation: an optimum approach for high quality multi scale image segmentation. In: Beutrage Zum AGIT-Symposium. Salzburg, Heidelberg, 2000. pp. 12–23.

Baumhoer, C.A., Dietz, A.J., Kneisel, C., Kuenzer, C., 2019. Automated extraction of antarctic glacier and ice shelf fronts from Sentinel-1 imagery using deep learning. Remote. Sens. 11 (21), 2529.

Belgiu, M., Csillik, O., 2018. Sentinel-2 cropland mapping using pixel-based and object-based time-weighted dynamic time warping analysis. Remote. Sens. Environ. 204, 509–523.

Beukema, J., Dekker, R., 2020. Half a century of monitoring macrobenthic animals on tidal flats in the Dutch Wadden Sea. Mar. Ecol. Prog. Ser. 656, 1–18.

Blaschke, T., 2010. Object based image analysis for remote sensing. ISPRS J. Photogramm. Remote. Sens. 65 (1), 2–16.

Chang, L., Stein, A., 2021. Exploring PAZ co-polarimetric SAR data for surface movement mapping and scattering characterization. Int. J. Appl. Earth Obs. Geoinf. 96, 102280.

Chen, C., Fu, J., Zhang, S., Zhao, X., 2019. Coastline information extraction based on the tasseled cap transformation of Landsat-8 OLI images. Estuar. Coast. Shelf Sci. 217, 281–291.

Chen, C., Sun, W., Yang, Z., Yang, G., Jia, M., Zhang, Z., Liang, J., Chen, Y., Ren, T., Hu, X., et al., 2024. Tracking dynamics characteristics of tidal flats using landsat time series and Google Earth Engine cloud platform. Resour. Conserv. Recycl. 209, 107751.

Chen, C., Tian, B., Wu, W., Duan, Y., Zhou, Y., Zhang, C., 2023a. UAV photogrammetry in intertidal mudflats: Accuracy, efficiency, and potential for integration with satellite imagery. Remote. Sens. 15 (7), 1814.

Chen, G., Weng, Q., Hay, G.J., He, Y., 2018. Geographic object-based image analysis (GEOBIA): Emerging trends and future opportunities. GIScience & Remote. Sens. 55 (2), 159–182.

Chen, C., Zhang, C., Tian, B., Wu, W., Zhou, Y., 2023b. Tide2Topo: A new method for mapping intertidal topography accurately in complex estuaries and bays with time-series Sentinel-2 images. ISPRS J. Photogramm. Remote. Sens. 200, 55–72.

Choi, C., Kim, D.j., 2018. Optimum baseline of a single-pass InSAR system to generate the best DEM in tidal flats. IEEE J. Sel. Top. Appl. Earth Obs. Remote. Sens. 11 (3), 919–929.

Chust, G., Galparsoro, I., Borja, A., Franco, J., Uriarte, A., 2008. Coastal and estuarine habitat mapping, using LiDAR height and intensity and multi-spectral imagery. Estuar. Coast. Shelf Sci. 78 (4), 633–643.

Collard, F., Ardhuin, F., Chapron, B., 2005. Extraction of coastal ocean wave fields from SAR images. IEEE J. Ocean. Eng. 30 (3), 526–533.

CWSS, 2020. Wadden sea world heritage. https://www.waddensea-worldheritage.org/our-world-heritage.

Da Silva, J.S., Calmant, S., Seyler, F., Rotunno Filho, O.C., Cochonneau, G., Mansur, W.J., 2010. Water levels in the Amazon basin derived from the ERS 2 and ENVISAT radar altimetry missions. Remote. Sens. Environ. 114 (10), 2160–2181.

Egbert, G.D., Bennett, A.F., Foreman, M.G., 1994. TOPEX/POSEIDON tides estimated using a global inverse model. J. Geophys. Research: Ocean. 99 (C12), 24821–24852.

Egbert, G.D., Erofeeva, S.Y., 2002. Efficient inverse modeling of barotropic ocean tides. J. Atmospheric Ocean. Technol. 19 (2), 183–204.

Elias, E., 2006. Morphodynamics of Texel inlet. IOS Press.

Elias, E.P., Van der Spek, A.J., Wang, Z.B., De Ronde, J., 2012. Morphodynamic development and sediment budget of the Dutch Wadden Sea over the last century. Neth. J. Geosci. 91 (3), 293–310.

Esch, T., Thiel, M., Bock, M., Roth, A., Dech, S., 2008. Improvement of image segmentation accuracy based on multiscale optimization procedure. IEEE Geosci. Remote. Sens. Lett. 5 (3), 463–467.

FitzGerald, D.M., 1996. Geomorphic variability and morphologic and sedimentologic controls on tidal inlets. J. Coast. Res. 23, 47–71.

Folmer, E.O., Bijleveld, A.I., Holthuijsen, S., van der Meer, J., Piersma, T., van der Veer, H.W., 2023. Space-time analyses of sediment composition reveals synchronized dynamics at all intertidal flats in the Dutch Wadden Sea. Estuar. Coast. Shelf Sci. 285, 108308.

Foresta, L., Gourmelen, N., Weissgerber, F., Nienow, P., Williams, J., Shepherd, A., Drinkwater, M.R., Plummer, S., 2018. Heterogeneous and rapid ice loss over the Patagonian Ice Fields revealed by CryoSat-2 swath radar altimetry. Remote. Sens. Environ. 211, 441–455.

Gao, E., Zhou, G., Li, S., Fu, B., Xiao, Y., Lan, Y., Wang, F., Xu, J., Zhu, Q., Bai, Y., 2024. Spatio-temporal evolution monitoring and analysis of tidal flats in Beibu Gulf from 1987 to 2021 using multi-source remote sensing. IEEE J. Sel. Top. Appl. Earth Obs. Remote. Sens..

Gorman, L., Morang, A., Larson, R., 1998. Monitoring the coastal environment; part IV: mapping, shoreline changes, and bathymetric analysis. J. Coast. Res. 14, 61–92.

Gräwe, U., Flöser, G., Gerkema, T., Duran-Matute, M., Badewien, T.H., Schulz, E., Burchard, H., 2016. A numerical model for the entire Wadden Sea: Skill assessment and analysis of hydrodynamics. J. Geophys. Research: Ocean. 121 (7), 5231–5251.

Hanssen, R.F., 2001. Radar interferometry: Data interpretation and error analysis. Kluwer Academic Publishers, Dordrecht.

Heidler, K., Mou, L., Baumhoer, C., Dietz, A., Zhu, X.X., 2021. HED-UNet: Combined segmentation and edge detection for monitoring the Antarctic coastline. IEEE Trans. Geosci. Remote. Sens. 60, 1–14.

Heygster, G., Dannenberg, J., Notholt, J., 2009. Topographic mapping of the German tidal flats analyzing SAR images with the waterline method. IEEE Trans. Geosci. Remote. Sens. 48 (3), 1019–1030.

Hossain, M.D., Chen, D., 2019. Segmentation for object-based image analysis (OBIA): A review of algorithms and challenges from remote sensing perspective. ISPRS J. Photogramm. Remote. Sens. 150, 115–134.

Jenks, G.F., 1967. The data model concept in statistical mapping. Int. Yearb. Cartogr. 7, 186–190.

Jia, M., Wang, Z., Mao, D., Ren, C., Wang, C., Wang, Y., 2021. Rapid, robust, and automated mapping of tidal flats in China using time series Sentinel-2 images and Google Earth Engine. Remote. Sens. Environ. 255, 112285.

Jordan, C., Visscher, J., Schlurmann, T., 2021. Projected responses of tidal dynamics in the North Sea to sea-level rise and morphological changes in the Wadden Sea. Front. Mar. Sci. 8, 685758.

Jung, R., Adolph, W., Ehlers, M., Farke, H., 2015. A multi-sensor approach for detecting the different land covers of tidal flats in the German Wadden Sea—A case study at norderney. Remote. Sens. Environ. 170, 188–202.

Kabat, P., Bazelmans, J., van Dijk, J., Herman, P.M., van Oijen, T., Pejrup, M., Reise, K., Speelman, H., Wolff, W.J., 2012. The Wadden Sea Region: Towards a science for sustainable development. Ocean. Coast. Manag. 68, 4–17.

Kalacska, M., Chmura, G., Lucanus, O., Bérubé, D., Arroyo-Mora, J., 2017. Structure from motion will revolutionize analyses of tidal wetland landscapes. Remote. Sens. Environ. 199, 14–24.

Kang, Y., Ding, X., Xu, F., Zhang, C., Ge, X., 2017. Topographic mapping on large-scale tidal flats with an iterative approach on the waterline method. Estuar. Coast. Shelf Sci. 190, 11–22.

Kim, S.W., Wdowinski, S., Amelung, F., Dixon, T.H., Won, J.-S., 2013. Interferometric coherence analysis of the Everglades wetlands, South Florida. IEEE Trans. Geosci. Remote. Sens. 51 (12), 5210–5224.

Lee, S.K., Ryu, J.H., 2017. High-accuracy tidal flat digital elevation model construction using TanDEM-X science phase data. IEEE J. Sel. Top. Appl. Earth Obs. Remote. Sens. 10 (6), 2713–2724.

Li, Z., Heygster, G., Notholt, J., 2014. Intertidal topographic maps and morphological changes in the German Wadden Sea between 1996–1999 and 2006–2009 from the waterline method and SAR images. IEEE J. Sel. Top. Appl. Earth Obs. Remote. Sens. 7 (8), 3210–3224.

Liu, C., Xiao, Y., Yang, J., 2017. A coastline detection method in polarimetric SAR images mixing the region-based and edge-based active contour models. IEEE Trans. Geosci. Remote. Sens. 55 (7), 3735–3747.

Lodder, Q.J., Wang, Z.B., Elias, E.P., van der Spek, A.J., de Looff, H., Townend, I.H., 2019. Future response of the Wadden Sea tidal basins to relative sea-level rise—an aggregated modelling approach. Water. 11 (10), 2198.

van Loon-Steensma, J.M., Schelfhout, H.A., Vellinga, P., 2014. Green adaptation by innovative dike concepts along the Dutch Wadden Sea coast. Environ. Sci. & Policy. 44, 108–125.

Mao, D., Wang, Z., Du, B., Li, L., Tian, Y., Jia, M., Zeng, Y., Song, K., Jiang, M., Wang, Y., 2020. National wetland mapping in China: A new product resulting from object-based and hierarchical classification of Landsat 8 OLI images. ISPRS J. Photogramm. Remote. Sens. 164, 11–25.

Mason, D., Davenport, I., Robinson, G., Flather, R., McCartney, B., 1995. Construction of an inter-tidal digital elevation model by the 'Water-Line' method. Geophys. Res. Lett. 22 (23), 3187–3190.

McFeeters, S.K., 1996. The use of the Normalized Difference Water Index (NDWI) in the delineation of open water features. Int. J. Remote. Sens. 17 (7), 1425–1432.

Murray, N.J., Phinn, S.R., DeWitt, M., Ferrari, R., Johnston, R., Lyons, M.B., Clinton, N., Thau, D., Fuller, R.A., 2019. The global distribution and trajectory of tidal flats. Nat. 565 (7738), 222–225.

Murray, N.J., Worthington, T.A., Bunting, P., Duce, S., Hagger, V., Lovelock, C.E., Lucas, R., Saunders, M.I., Sheaves, M., Spalding, M., et al., 2022. High-resolution mapping of losses and gains of Earth's tidal wetlands. Sci. 376 (6594), 744–749.

Nederhoff, K., Saleh, R., Tehranirad, B., Herdman, L., Erikson, L., Barnard, P.L., Van der Wegen, M., 2021. Drivers of extreme water levels in a large, urban, high-energy coastal estuary–A case study of the San Francisco Bay. Coast. Eng. 170, 103984.

Niedermeier, A., Hoja, D., Lehner, S., 2005. Topography and morphodynamics in the German Bight using SAR and optical remote sensing data. Ocean. Dyn. 55 (2), 100–109.

Oliver, M.A., Webster, R., 1990. Kriging: a method of interpolation for geographical information systems. Int. J. Geogr. Inf. Syst. 4 (3), 313–332.

Reise, K., Baptist, M., Burbridge, P., Dankers, N., Fischer, L., Flemming, B., Oost, A., Smit, C., 2010. The Wadden Sea-a universally outstanding tidal wetland. In: The Wadden Sea 2010. Common Wadden Sea Secretariat (CWSS); Trilateral Monitoring and Assessment Group: Wilhelmshaven.(Wadden Sea Ecosystem; 29/Editors, Harald Marencic and Jaap de Vlas), vol. 7.

Robusto, C.C., 1957. The cosine-haversine formula. Am. Math. Mon. 64 (1), 38–40.

Salameh, E., Frappart, F., Turki, I., Laignel, B., 2020. Intertidal topography mapping using the waterline method from Sentinel-1 &-2 images: The examples of Arcachon and Veys Bays in France. ISPRS J. Photogramm. Remote. Sens. 163, 98–120.

Shao, W., Zhao, C., Jiang, X., Sun, Z., Wang, X., Wang, J., Cai, L., 2021. Characteristics of suspended sediment in Sentinel-1 synthetic aperture radar observations. Remote. Sens. Lett. 12 (11), 1167–1179.

Soares, F., Catalão, J., Nico, G., 2012. Using K-Means and morphological segmentation for intertidal flats recognition. In: 2012 IEEE International Geoscience and Remote Sensing Symposium. IEEE, pp. 764–767.

Tong, S.S., Deroin, J.P., Pham, T.L., 2020. An optimal waterline approach for studying tidal flat morphological changes using remote sensing data: A case of the northern coast of Vietnam. Estuar. Coast. Shelf Sci. 236, 106613.

Van Prooijen, B.C., Tissier, M.F., De Wit, F.P., Pearson, S.G., Brakenhoff, L.B., van Maarseveen, M.C., van der Vegt, M., Mol, J.W., Kok, F., Holzhauer, H., et al., 2020. Measurements of hydrodynamics, sediment, morphology and benthos on Ameland ebb-tidal delta and lower shoreface. Earth Syst. Sci. Data. 12 (4), 2775–2786.

Wang, Z.B., Elias, E.P., van der Spek, A.J., Lodder, Q.J., 2018a. Sediment budget and morphological development of the Dutch Wadden Sea: impact of accelerated sea-level rise and subsidence until 2100. Neth. J. Geosci. 97 (3), 183–214.

Wang, L., Marzahn, P., Bernier, M., Ludwig, R., 2018b. Mapping permafrost landscape features using object-based image classification of multi-temporal SAR images. ISPRS J. Photogramm. Remote. Sens. 141, 10–29.

Wang, X., Xiao, X., Zou, Z., Chen, B., Ma, J., Dong, J., Doughty, R.B., Zhong, Q., Qin, Y., Dai, S., et al., 2020. Tracking annual changes of coastal tidal flats in China during 1986–2016 through analyses of Landsat images with Google Earth Engine. Remote. Sens. Environ. 238, 110987.

van Weerdenburg, R., Pearson, S., van Prooijen, B., Laan, S., Elias, E., Tonnon, P.K., Wang, Z.B., 2021. Field measurements and numerical modelling of wind-driven exchange flows in a tidal inlet system in the Dutch Wadden Sea. Ocean. Coast. Manag. 215, 105941.

Wu, W., Zhang, M., Chen, C., Chen, Z., Yang, H., Su, H., 2024. Coastal reclamation shaped narrower and steeper tidal flats in Fujian, China: Evidence from time-series satellite data. Ocean. Coast. Manag. 247, 106933.

Yang, J., Tan, K., Liu, S., Zhang, W., Tao, P., 2023. Inshore marine litter detection using radiometric and geometric data of terrestrial laser scanners. Int. J. Appl. Earth Obs. Geoinf. 116, 103149.

Zhang, B., Chang, L., Stein, A., 2021a. Spatio-temporal linking of multiple SAR satellite data from medium and high resolution Radarsat-2 images. ISPRS J. Photogramm. Remote. Sens. 176, 222–236.

Zhang, B., Chang, L., Stein, A., 2022a. A model-backfeed deformation estimation method for revealing 20-year surface dynamics of the Groningen gas field using multi-platform SAR imagery. Int. J. Appl. Earth Obs. Geoinf. 111, 102847.

Zhang, E., Liu, L., Huang, L., Ng, K.S., 2021b. An automated, generalized, deep-learning-based method for delineating the calving fronts of Greenland glaciers from multi-sensor remote sensing imagery. Remote. Sens. Environ. 254, 112265.

Zhang, S., Xu, Q., Wang, H., Kang, Y., Li, X., 2022b. Automatic Waterline Extraction and Topographic Mapping of Tidal Flats From SAR Images Based on Deep Learning. Geophys. Res. Lett. 49 (2), e2021GL096007.